

Coherent Dijets in Ultra-peripheral Pb+Pb Collisions at

$$\sqrt{s_{NN}} = 5.02 \text{ TeV}$$

By

Samuel Boren

Submitted to the graduate degree program in Department of People who read Abstracts and the Graduate Faculty of the University of Kansas in partial fulfillment of the requirements for the degree of Doctor of Philosophy.

Committee members

MEMBER 1, Chairperson

MEMBER 2, Occasional Visitor

MEMBER 3

MEMBER 4, The One Who Never Answers Email

The One with an Extra Long Name

The Fifth Beatle

Date defended: October 02, 2016

The Thesis Committee for Samuel Boren certifies
that this is the approved version of the following thesis :

Coherent Dijets in Ultra-peripheral Pb+Pb Collisions at $\sqrt{s_{NN}} = 5.02$ TeV

MEMBER 1, Chairperson

Date approved: October 06, 2016

Abstract

Acknowledgements

Contents

1	Ultra-relativistic heavy-ion collisions	1
1.1	The Standard Model	1
1.2	Quantum Electrodynamics	2
1.3	Quantum Chromodynamics	3
1.4	QCD Experiments	4
1.4.1	Scattering as a Tool	4
1.4.2	Deep Inelastic Scattering	5
1.4.3	Quark Gluon Plasma	7
2	Ultra-peripheral Collisions at the Large Hadron Collider	9
2.1	Ultra-peripheral Heavy-Ion Collisions	9
2.2	Vector Meson Photoproduction	11
2.3	Photon-Photon Interactions	11
2.4	Dijet Photoproduction	12
2.4.1	Factorization	13
2.4.2	Wigner Distribution	17
3	The Experiment	20
3.1	Large Hadron Collider	20
3.1.1	ATLAS	20
3.1.2	ALICE	21
3.1.3	LHCb	21
3.1.4	TOTEM	21

3.2	Compact Muon Solenoid	21
3.2.1	Tracker	22
3.2.1.1	Pixel Tracker	24
3.2.1.2	Strip Tracker	24
3.2.2	Electromagnetic Calorimeter	24
3.2.3	Hadronic Calorimeter	26
3.2.3.1	Hadronic Forward Calorimeters	28
3.2.4	Muon Detector	28
3.2.5	Zero Degree Calorimeter	29
3.2.6	Particle Flow Algorithm	29
4	Measuring Luminosity	31
4.1	Instantaneous Luminosity	31
4.2	Luminometers	31
4.3	Van de Meer Scanning Calibration	32
4.4	Comparative Luminosity Performance of LHC Detectors	33
4.5	Systematic Uncertainty	33
4.6	My Contributions	33
5	Trigger Development and Performance	36
5.1	Introduction to Triggering	36
5.2	Triggering at CMS	36
5.3	My Contributions	38
6	Data Analysis	39
7	Systematic Uncertainties	40
8	Results and Conclusions	41

List of Figures

1.1	QED Components of Feynman Diagrams.	3
1.2	QCD Coupling Constant vs. Q^2	5
1.3	Collision Cross Section vs Bjorken-x, theory and data [1].	6
1.4	QCD Phase Diagram.	8
2.1	(a.) electromagnetic field of stationary charge (b.) eletromagnetic field of boosted charge [2].	9
2.2	γ +proton $\rightarrow J/\Psi$ +proton cross-section.	11
2.3	Pat Kenny Plot 1	12
2.4	Pat Kenny Plot 2	12
2.5	Pat Kenny Plot 3	13
2.6	Event Display of ATLAS photon-photon scattering	14
2.7	Feynman diagrams for coherent jet photoproduction in (upper a.) lepton-proton collisions, (upper b.) Pb-Pb collisions, (lower a.) direct-photon in ep, (lower b.) resolved-photon in ep.	15
2.8	Ratio of H1 data cross-section to NLO-QCD cross-section.	16
2.9	Beam envelope vs. distance to vertex in H1.	17
2.10	Subnuclear tomography	18
2.11	Interconnectedness of Parton Distributions.	19
2.12	Feynman Diagram of Coherent Dijets in Dipole Framework.	19
3.1	CMS Detector	22
3.2	CMS radial cross-section	23
3.3	Pseudorapidity acceptance of tracker	23

3.4	ECAL components	25
3.5	Ecal energy resolution	25
3.6	Ecal energy resolution	26
3.7	HCAL energy resolution	27
3.8	HCAL Components	27
3.9	Pseudorapidity acceptance of muon detector	29
3.10	Performance of particle flow algorithm compared to calorimeter readout.	30
4.1	PCC VdM Scans.	32
4.2	CMS lumi during HI-2015.	33
4.3	CMS Lumi by Era.	34
4.4	Systematic Uncertainty During 2015 pp Run.	34
4.5	Luminosity by CMS fill.	35
5.1	High multiplicity PbPb collision	37
5.2	UPC Upsilon candidate	37
5.3	UPC Upsilon candidate	38
5.4	Example of trigger rate.	38

List of Tables

Chapter 1

Ultra-relativistic heavy-ion collisions

1.1 The Standard Model

The Standard Model describes the fundamental particles of the universe in terms of fermions and bosons. Fermions are particles with half-integer spin, while bosons have integer-spin. This difference in spin has far reaching consequences. Fermions must obey the Pauli Exclusion Principle: only one fermion at a time can occupy a given state. However, multiple bosons can simultaneously occupy a specific state.

Among the fermions are the leptons, neutrinos, and quarks. The leptons consist of the electron, muon, and tau, as well as their anti-particles. The leptons are seemingly fundamental: high energy experiments have yet to observe internal lepton-structure. Neutrinos are weakly interacting particles detected primarily through the precise measuring of missing transverse energy in the products of particle collisions. Quarks are the constituent particles of baryons, which contain three valence quarks, and mesons, which contain two valence quarks. In addition to the valence quarks are the sea quarks, which appear and disappear as quark-antiquark pairs within hadrons. The hadrons are particles made of quarks and gluons. Gluons are particles that mediate the strong nuclear force; likewise, photons mediate the electromagnetic force, and weak-gauge bosons mediate the weak nuclear force. A fourth boson, the graviton, is expected to transmit the gravitational force, but this particles existence has not been verified.

The behavior of fundamental particles is best described within the framework of quantum field theory (QFT). QFT defines a Lagrangian for fundamental particles. This Lagrangian then predicts the outcome of particle collisions. Different terms in the Lagrangian correspond to the various

interactions between particles. The Standard Model Lagrangian, $\mathcal{L}_{StandardModel}$ can be broken down into three basic terms:

$$\mathcal{L}_{StandardModel} = \mathcal{L}_{QED} + \mathcal{L}_{QCD} + \mathcal{L}_{Higgs} + \dots, \quad (1.1)$$

Where \mathcal{L}_{QED} is the QED Lagrangian, \mathcal{L}_{QCD} is the QCD Lagrangian, and \mathcal{L}_{Higgs} is the Higgs Lagrangian. The QED and QCD Lagrangians will be the most important in what follows [3].

The most accessible approach to quantum field theory is through the use of Feynman diagrams. First, one imagines an interaction between particles. Then, one draws this process into a Feynman diagram, which is essentially a pictorial representation of exchanges between particles. The Lagrangian can be interpreted into Feynman rules. These rules describe how the Feynman diagram translates into a calculation for the quantum mechanical amplitude of the process. The quantum mechanical amplitude, in turn, is proportional to the cross-section of the process. This is important because, since the cross-section is invariant between experiments, one can use it to effectively test for invariant quantities in the Lagrangian [4].

1.2 Quantum Electrodynamics

Quantum electrodynamics (QED) is a theory of electromagnetic interaction in terms of relativistic quantum field theory. QED addresses three specific processes: photon motion, electron motion, and the emission, or absorption, of a photon by an electron. To do this, first a Lagrangian is established based on Maxwell's laws and quantum mechanics. The photon constitutes a spin-1 solution to Maxwell's equations. Likewise, electrons are described, at non-relativistic scales, by the Schrodinger equation, at relativistic scales by the Dirac equation. Figure 1.1 shows the resulting processes allowed by QED: the translation of an electron, the translation of a photon, and the scattering of a photon off an electron [5].

The QED coupling constant, α_{QED} , is approximately $1/137$ at perturbative scales. However,

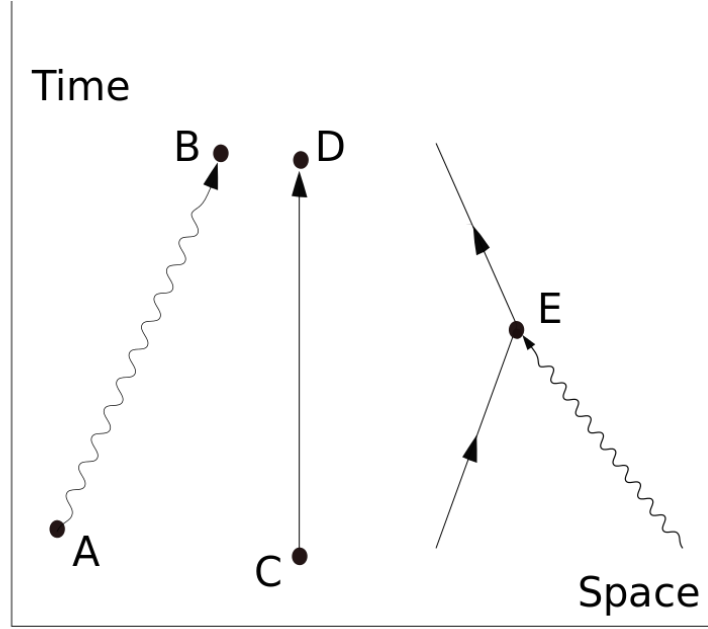


Figure 1.1: QED Components of Feynman Diagrams.

at small scales, i.e. non-perturbative momentum transfers Q^2 , the coupling constant increases:

$$\alpha_{QED}(Q^2) = \frac{\alpha_{em}}{(1 - \frac{\alpha_{em}}{3\pi}) \ln(\frac{Q^2}{m^2})}, \quad (1.2)$$

where $\alpha_{QED}(Q^2)$ is the QED coupling constant at high Q^2 , α_{em} , and m is the electron mass. High values of Q^2 are non-perturbative because, at small scales and high momentum, the fluctuation of photons into electron-positron pairs begins to saturate.

1.3 Quantum Chromodynamics

The quarks are a family of fermions that compose the baryons and the mesons. Baryons consist of three quarks in a color neutral state, while mesons consist two quarks in a color neutral state. "Color" in this context refers to the six kinds of strongly-interacting charge available to quarks: red and anti-red, blue and anti-blue, and green and anti-green. Color charge has no relation to optical phenomena, but provides a useful analogy for the stable combinations of quarks. The net color-

charge of a baryon or meson is colorless. By way of analogy, a red quark, green quark, and blue quark can together form a hadron, in the way that conventional red, green, and blue can together form white [6].

Gluons are the QCD analogues of the photons in QED. Gluons are spin-1 and massless, but unlike photons, which do not carry electromagnetic charge, gluons carry strongly-interacting charge: color. Color comes six varieties: red, antired, blue, antiblue, green, and antigreen [7].

Unlike QED, the QCD coupling increases with distance [1]. Figure 1.2 shows the running of the QCD coupling with Q^2 :

$$\alpha_{QCD}(Q^2) = \frac{4\pi}{(11 - \frac{2}{3}n_f)\ln(\frac{Q^2}{\Lambda_{QCD}^2})}, \quad (1.3)$$

where n_f is the number of quark flavors, Q^2 is the momentum transfer, and Λ_{QCD}^2 is the mass scale. This has the practical consequence of the strong-interactions being stronger in high momentum transfer collisions. The direct results of the running QCD coupling are the dual phenomena of asymptotic freedom and color confinement. At large distances, string tension describes the binding force of the quarks. At short distances, however, Coulomb-like interactions dominate. The QCD coupling constant can be measured via the cross-section of inelastic proton-proton collisions, and also the cross section of electron-positrons into triple jets.

Within the nucleus, a proton can be thought of as a bubble in a vacuum. Debye screening exerts a pressure on the proton. This pressure is responsible for the size of the proton.

1.4 QCD Experiments

1.4.1 Scattering as a Tool

Scattering experiments are the basic tool for exploring the nucleus. The Large Hadron Collider (LHC) is capable of reaching heavy-ion collision energies of up to 7 TeV per nucleon-nucleon. The higher the energy, the more experiments can probe the nuclear phase-space diagram. Momentum transferred, expressed as Q^2 , is an important quantity for characterizing QCD measurements. In

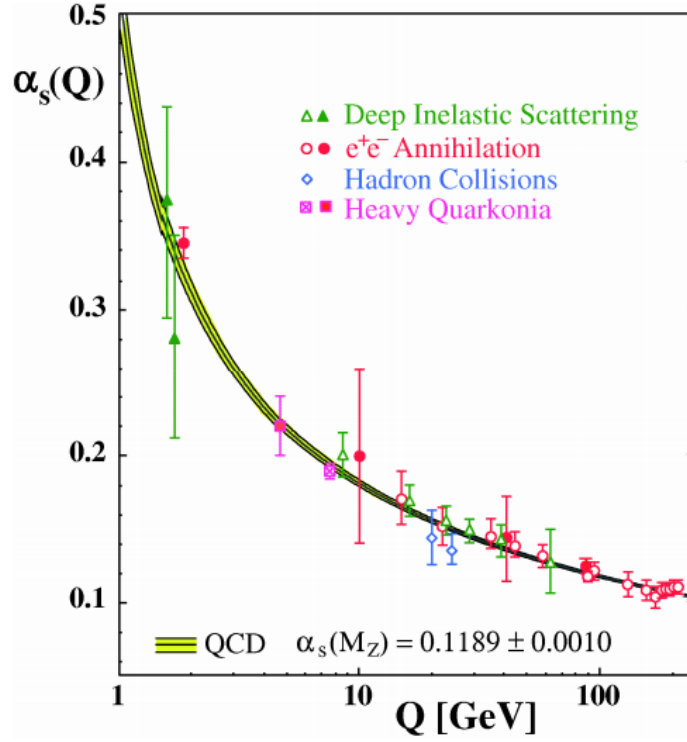


Figure 1.2: QCD Coupling Constant vs. Q^2 .

addition to Q^2 , Bjorken- x , also known as Bjorken-scaling is necessary to describe the nuclear phase space. Bjorken- x represents the momentum fraction of partons [8].

At the turn of the century, Ernst Rutherford probed the gold atom by bombarding a gold sheet with alpha-particles, i.e. helium nuclei. The angular distribution of the scattered alpha-particles demonstrates that the mass of the atom is concentrated in a small volume, i.e, the atom is mostly empty space. Further expedriments revealed that the atomic nuclei consisted of separate positively and neutrally charged particles: protons and neutrons.

1.4.2 Deep Inelastic Scattering

Deep inelastic scattering commonly refers to the scattering of a leptons off hadrons. Experiments at HERA focused on electron-proton collisions. In these collisions, the electron was used as a source of photons and neutrinos. When these particles scatter off the proton, the dependence of the collision cross section, on momentum transfer and scattering angle of the source electron, reflects

the structure of the proton. These experiments provided the first evidence of two phenomena: the parton model and Bjorken-scaling.

The parton model, first proposed by Richard Feynman, posits that hadrons in general, and nucleons in specific, are made of more fundamental constituent particles which may or may not be the quarks implied by the SU(3) symmetry. In addition to the quarks, the partons also include any field quanta associated with nuclear forces. In time, these field quanta are dubbed "gluons".

"Scaling" is an interpretation of the data from deep inelastic scattering (DIS). First proposed by James Bjorken, scaling is reflected in the incoherence of photon-proton interactions at photon energies above $1 \text{ GeV}/c$. Predictions from perturbative QCD are in good agreement with DIS data from HERA, as seen in figure 1.3. In this graph the Bjorken- x momentum fraction is designated x , and σ_r represents the F_2 structure function, and Q^2 is the transferred momentum from the electron to the proton. The order of magnitude of σ_r set by the Bjorken- x .

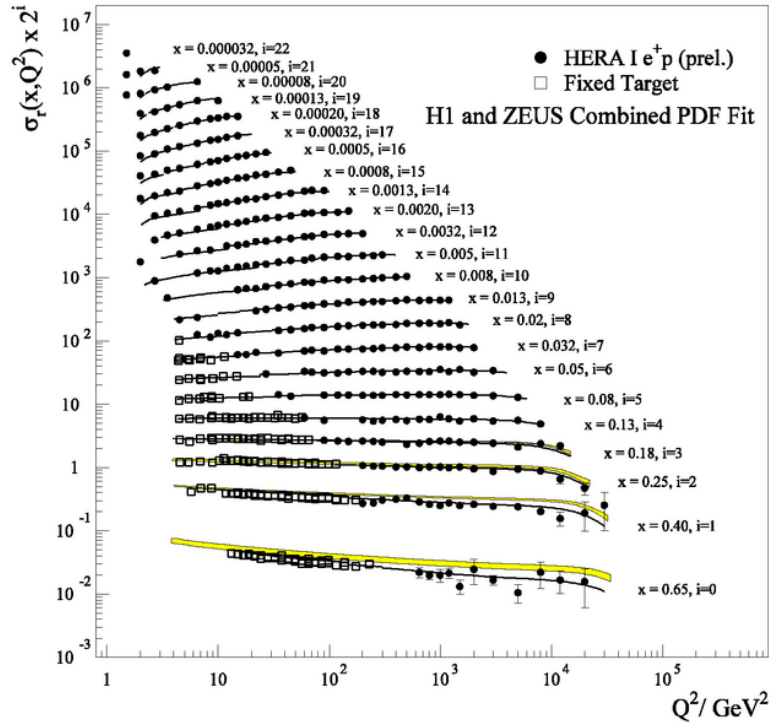


Figure 1.3: Collision Cross Section vs Bjorken- x , theory and data [1].

At the small scales probed by high energy photons, the decreasing QCD coupling causes quarks and gluons to interact weakly. This phenomena is called "asymptotic freedom". Because gluons

themselves carry color charge, the gluons about a quark tend to have an anti-screening behavior: the gluon color adds to the quark color, increasing the net color charge of the area. At smaller distances to a quark, then, there are fewer and fewer gluons augmenting the color interaction.

1.4.3 Quark Gluon Plasma

The modern understanding of subnuclear physics is based on results from three laboratories: Lawrence Berkeley National Laboratory (LBNL), Brookhaven National Laboratory (BNL), and CERN. Fixed target experiments hinted at the existence of a quark gluon plasma, but the collision energies were too low for this state to last. These experiments confirmed the developing model of the QCD phase space; see figure 1.4. Essentially, quark matter organizes itself differently depending on temperature and baryon density. At low energies, quark matter exists in bound states: the hadrons. However, in the high energy limit, quarks and gluons take the form of a strongly interacting plasma: the quark-gluon plasma (QGP). The QGP represents the extreme case of asymptotic freedom; the QCD coupling constant becomes small enough that quarks and gluons no longer behave as bound states. There are two ways of achieving the high energies necessary to form QGP. High baryon densities cause the quarks of separate hadrons to interact at small distances where asymptotic freedom takes effect. It is not currently possible to achieve these densities in laboratory experiments, though this state is thought to occur in neutron stars. By contrast, particle collider's like the LHC increase the energy density by colliding heavy-ions at ultra-relativistic velocities. The high temperature environment thus produced manifests QGP. The early universe, mere milliseconds after the Big Bang, is thought to have existed as QGP.

There are a number of experimental signatures of QGP. Of particular interest are charm suppression and strangeness enhancement, elliptic flow, jet quenching. The QGP is thought to suppress the production of J/Ψ mesons in heavy-ion collisions. The predicted viscosity of QGP would cause elliptic flow in the overlap region of heavy-ion collisions. Lastly, hadronic jets would interact strongly with the QGP; therefore, dijets will have significant energy imbalance depending on the multiple interactions of the components jet with the QGP. All of these cases require a good

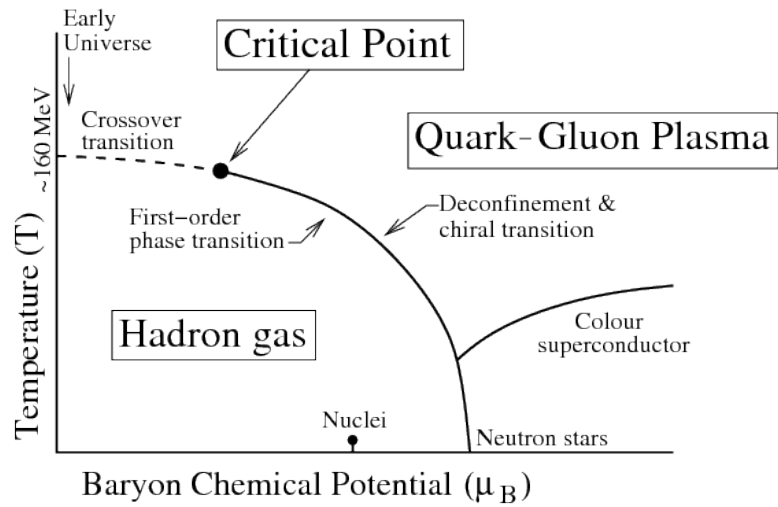


Figure 1.4: QCD Phase Diagram.

understanding the heavy-ion initial state as a basis for comparison.

Chapter 2

Ultra-peripheral Collisions at the Large Hadron Collider

2.1 Ultra-peripheral Heavy-Ion Collisions

Similar to the Rutherford experiment, in heavy-ion collisions the scattered particles carry information about the internal structure of the nucleus.

The Rutherford experiment has the three components that still characterize high-energy nuclear experiments: a probe, a medium, and a signal. Alpha particles probe the medium of the gold atom, and the angular distribution of scattered alpha particles signals the internal structure of the atom.

Ultra-peripheral collisions occur at impact parameters greater than the sum of the heavy-ion radii. In these collisions, hadronic interactions are strongly suppressed while photonuclear activity is enhanced proportional to the square of the nuclear charge. The electromagnetic field of an incoming heavy-ion, from the perspective of a target, is equivalent to a flux of virtual photons; figure 2.1 illustrates the Lorentz contraction of the field of a boosted charge.

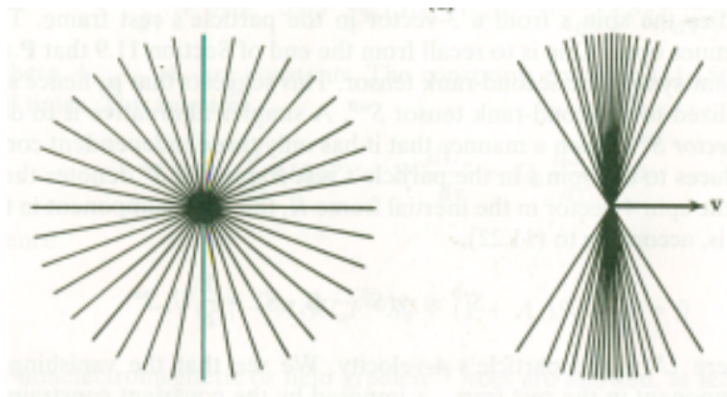


Figure 2.1: (a.) electromagnetic field of stationary charge (b.) electromagnetic field of boosted charge [2].

The Weizsacker-Williams approximation (WWA) calculates the density of photons, about the nucleus, as a function of energy. WWA is a semi-classical formulation. Maxwell's equations are solved for a stationary point charge boosted to an ultra-relativistic velocity. In the target's frame, the Fourier transform of the source field is taken. The Fourier frequency modes are interpreted through the quantum mechanical equation of photon energy. The photon flux as function of energy is given by

$$N(\omega, b) = \frac{\alpha}{\hbar\omega} \left(\frac{Z}{b\beta\pi} \right)^2 \left(\frac{\omega b}{\gamma v} \right) K_1^2 \left(\frac{\omega b}{\gamma v} \right), \quad (2.1)$$

where α is the QED coupling constant, ω is the photon energy, Z is the atomic number of the nuclei, b is the impact parameter, β is ratio of the nuclei speed to the speed of light, γ is the Lorentz boost of the nuclei, K_1^2 is a Bessel function, v is the photon frequency [2].

Gluons are the particle exchanged in strong interactions. However, gluons themselves carry color charge. By analogy, photons transmit the electromagnetic force, but do not themselves have an electric charge. The gluons are spin-1, meaning that more than one can occupy the same quantum state.

When a quark is scattered from a nucleus, the strong force field lines for a tube between the quark and its counterpart. Given that the strong coupling constant increases with distance the strong interaction gathers potential energy until the threshold for quark production is passed, at which point an anti-quark is generated to screen the ejected quark. These quarks continue to separate from each other and continue the quark generation process. The resulting final state hadron distribution takes the form of a cone centered on the path of the initial quark.

QCD factorisation describes the diffractive-photoproduction dijet cross-section as the convolution of the partonic cross-section with the diffractive parton distributions. However, factorisation only describes H1 data if the resolved-photon contribution is suppressed.

The photoproduction cross-section is proportional to the gluon distribution. At low momentum transfer, photons interact electromagnetically, i.e. directly, with partons. High energy, "resolved" photons possess a hadronic structure; instead of directly interacting with the nuclei, these photons fluctuate into mediating quark-antiquark pairs.

2.2 Vector Meson Photoproduction

The virtual photons present in UPC can fluctuate into a quark-antiquark pair which can take the form of a low mass meson. This meson then interacts with the target nuclei via colorless gluon exchange, emitting a vector meson. If the virtual photon interacts coherently with the target nucleus, this is reflected in the transverse momentum of the vector meson. The vector meson decays into a dilepton pair detectable by CMS.

Ultra-peripheral coherent J/Ψ photoproduction was studied in the ALICE 2011 Pb-Pb data.

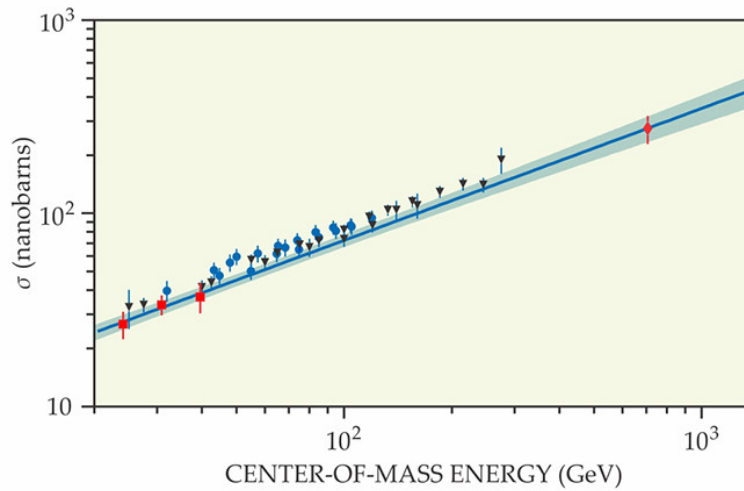


Figure 2.2: $\gamma + \text{proton} \rightarrow J/\Psi + \text{proton}$ cross-section.

CMS has studied J/Ψ and ρ photoproduction off the proton in proton-Pb collisions.

2.3 Photon-Photon Interactions

Classical electrodynamics forbids the scattering of a photon off another photon.

The polarization of the vacuum is a consequence of quantum mechanics. Around a photon there is a cloud of particle-antiparticle pairs, appearing together and then annihilating each other after a time proportional to their energy. In so far as these particles have an electric charge, portions of the local area may carry a non-zero electric charge. Thus, two photons may scatter off each other in three possible exchanges: Diagrams for Delbrück scattering, photon splitting, and elastic

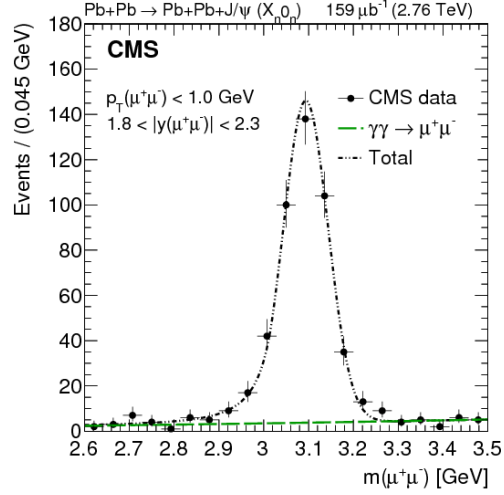


Figure 2.3: Pat Kenny Plot 1

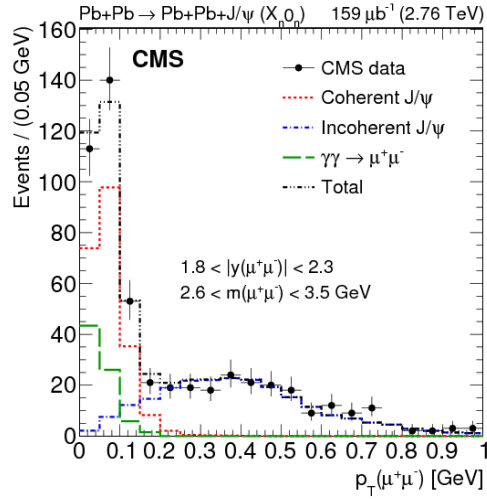


Figure 2.4: Pat Kenny Plot 2

light-by-light scattering.

2.4 Dijet Photoproduction

The dijet photoproduction cross-section, like that of vector meson photoproduction, displays diffractive dips in its $|t|$ dependence. Furthermore, according to the color glass condensate formalism, coherent dijet production is sensitive to gluon saturation effects at small Bjorken- x values. Gluon

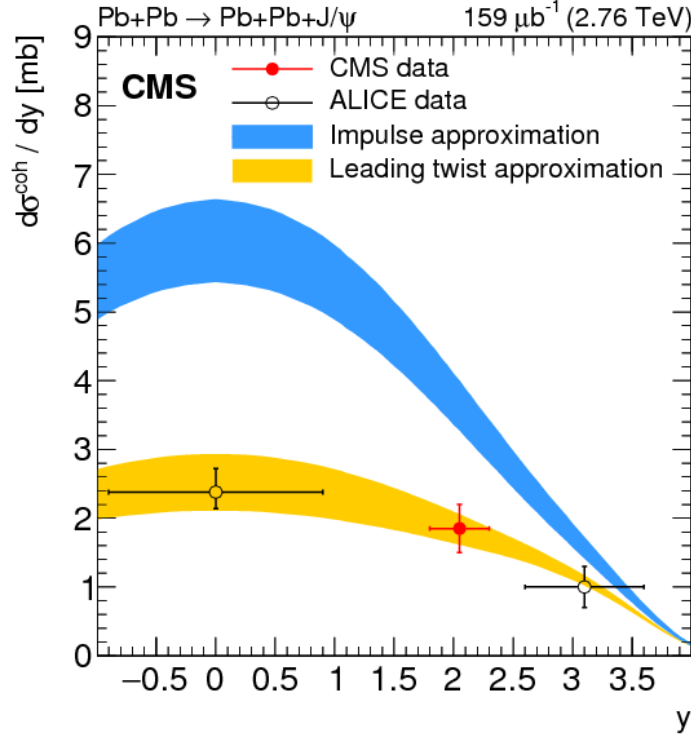


Figure 2.5: Pat Kenny Plot 3

saturation would affect the color-dipole orientation of nucleons in the transverse plane. This effect should be reflected in an enhanced azimuthal angle correlation of the jets.

2.4.1 Factorization

Diffraction dijet photoproduction is not describable in perturbative QCD. For coherent processes the photon energy is small, and therefore the wavelength is large compared to the size of the nucleus. At these large distances, there isn't a hard scale, and so perturbation calculations cannot be done. Gluon splitting interactions dominate the low Bjorken- x partons. QCD collinear factor-

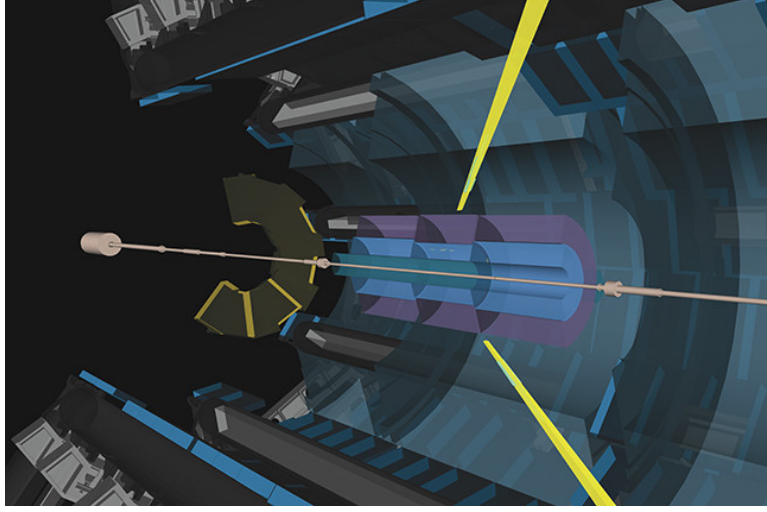


Figure 2.6: Event Display of ATLAS photon-photon scattering

ization describes these soft interactions via the convolution of parton cross sections, taken from perturbative QCD, and diffractive parton distribution functions, taken from experiment [9].

In electron-hadron collisions, diffractive photoproduction is characterized by the presence of a large rapidity gap in the final state and an intact nucleus. The Feynman diagram of electroproduction in lepton-hadron collisions is similar to that of photoproduction in ultraperipheral collisions, as seen in fig.2.7. The diffractive dijet cross section is expressed by the convolution of partonic cross sections $d\hat{\sigma}$ and diffractive PDFs $f_{i/p}^D$.

$$d\sigma(ep \rightarrow e + 2jets + X' + p) = \sum_i \int dt \int dx_{\mathbb{P}} \int dz_{\mathbb{P}} d\hat{\sigma}_{ei \rightarrow 2jets}(\hat{s}, \mu_R^2, \mu_F^2) \times f_{i/p}^D(z_{\mathbb{P}}, \mu_F^2, x_{\mathbb{P}}, t), \quad (2.2)$$

where $x_{\mathbb{P}}$ is longitudinal momentum fraction lost by the incoming proton, $d\hat{\sigma}_{ei \rightarrow 2jets}$ is the partonic cross-section for the process, $z_{\mathbb{P}}$ is the longitudinal momentum fraction of the pomeron entering the hard process, \hat{s} is the squared invariant energy of the subprocess, μ_R^2 is the squared renormalization scale, μ_F^2 is the squared factorisation scale, $f_{i/p}^D$ is the diffractive parton distribution, and t is the four-momentum transfer squared at the vertex.

In the proton-vertex factorisation hypothesis, the dependence on $x_{\mathbb{P}}$ and $|t|$ is factored out of the dependence on μ_F^2 and $z_{\mathbb{P}}$. Furthermore, $f_{i/p}^D$ is sum of contributions from the pomeron and

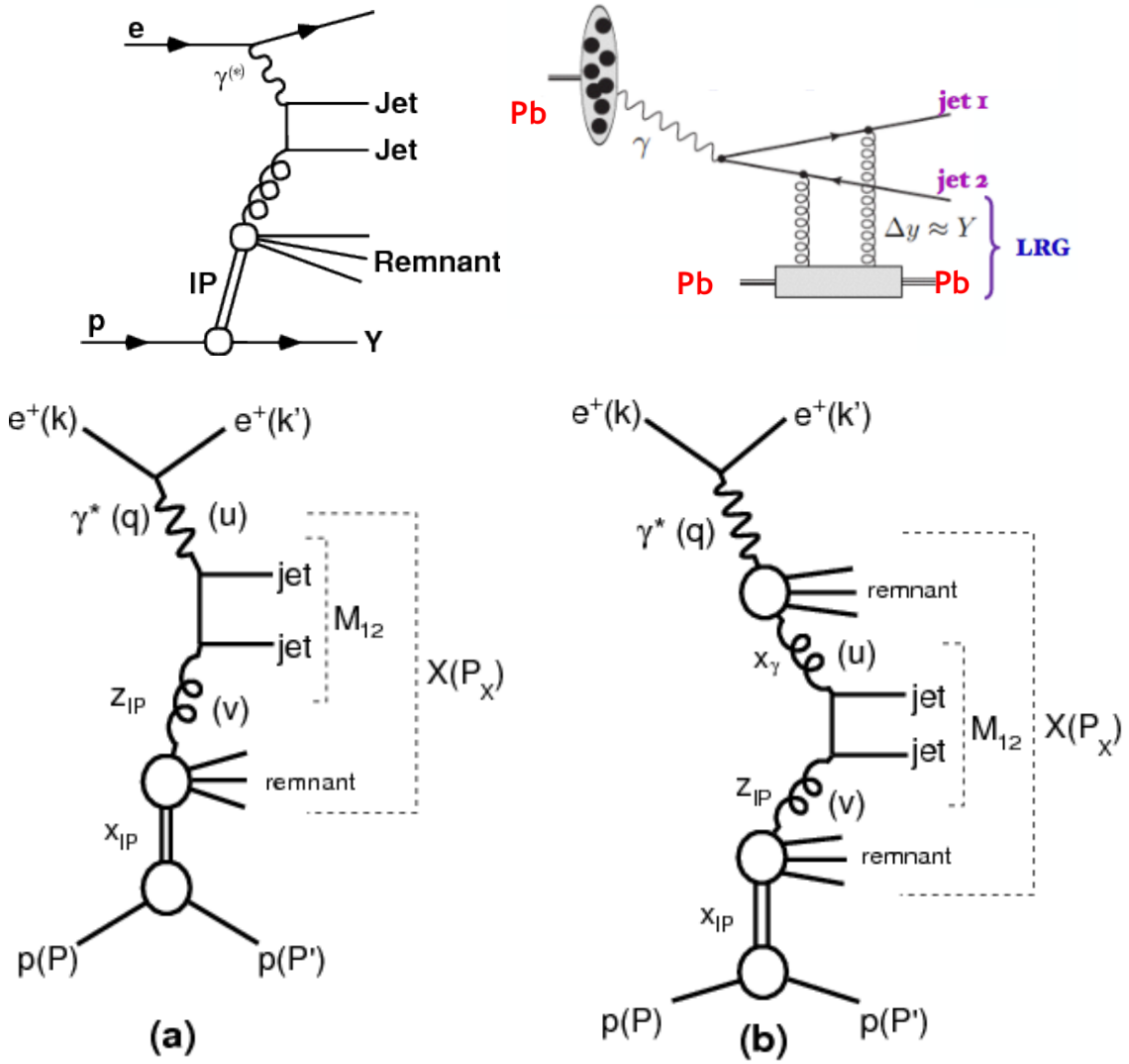


Figure 2.7: Feynman diagrams for coherent jet photoproduction in (upper a.) lepton-proton collisions, (upper b.) Pb-Pb collisions, (lower a.) direct-photon in ep, (lower b.) resolved-photon in ep.

Reggeon:

$$f_{i/p}^D(z_{\mathbb{P}}, \mu_F^2, x_{\mathbb{P}}, t) = f_{\mathbb{P}/p}(x_{\mathbb{P}}, t) f_{i/\mathbb{P}}(z_{\mathbb{P}}, \mu_F^2) + n_{\mathbb{R}} f_{\mathbb{R}/p}(x_{\mathbb{P}}, t) f_{i/\mathbb{R}}(z_{\mathbb{P}}, \mu_F^2), \quad (2.3)$$

where \mathbb{P}/p is the pomeron flux factor, $f_{\mathbb{R}/p}$ is the Reggeon flux factor, $n_{\mathbb{R}}$ is the normalization factor of the Reggeon, $f_{i/\mathbb{P}}$ is the pomeron parton distribution, and $f_{i/\mathbb{R}}$ is the Reggeon parton distribution.

Lepton-hadron collisions were performed at HERA and measured by the H1 experiment. These experiments reported a value for the total diffractive photoproduction cross section that is double

that predicted by QCD collinear factorization; fig.2.8 compares the cross-section of H1 data to that predicted by NLO-QCD. Diffractive events were selected for using rapidity gaps or the presence of leading protons in the very forward proton spectrometer (VFPS).

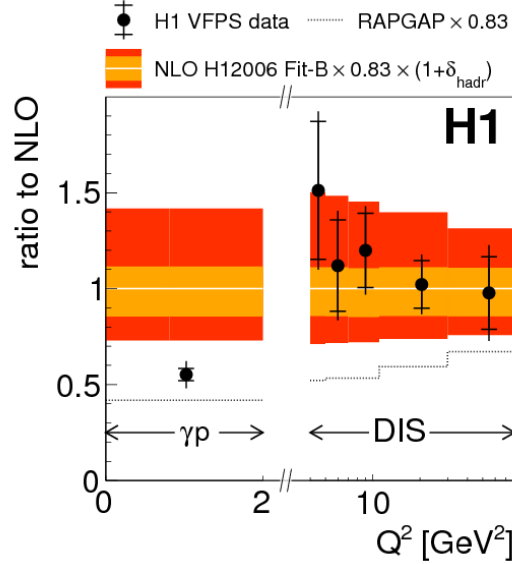


Figure 2.8: Ratio of H1 data cross-section to NLO-QCD cross-section.

H1 used the Very Forward Proton Spectrometer (VFPS) to trigger on low Q^2 protons. The VFPS consists of two Roman Pots located 218 m and 222 m from the H1 interaction-point in the forward direction. The VFPS can detect protons scattered at very low transverse momentum, corresponding to $0.008 < x_P < 0.028$ and $|t| < 0.6$. Each of the Roman Pots contains layers of scintillating fibers, which are covered by a layer of scintillator tiles. The fibers readout to photomultipliers, and the tiles both shield from radiation and trigger on protons. The track efficiency of VFPS is a remarkable 96%, and the background contamination is kept at 1% , making the detector excellent for studying diffractive events. Figure 2.9 shows the $|t|$ coverage of the Forward Proton Spectrometer (FPS) and VFPS.

The H1 data was compared to predictions based on NLO-QCD convoluted with diffractive parton distribution functions (DPDFs) from HERA inclusive diffractive deep-inelastic scattering (DDIS) data. For diffractive pp collisions the high transverse momentum jets yield a hard scale for perturbative QCD.

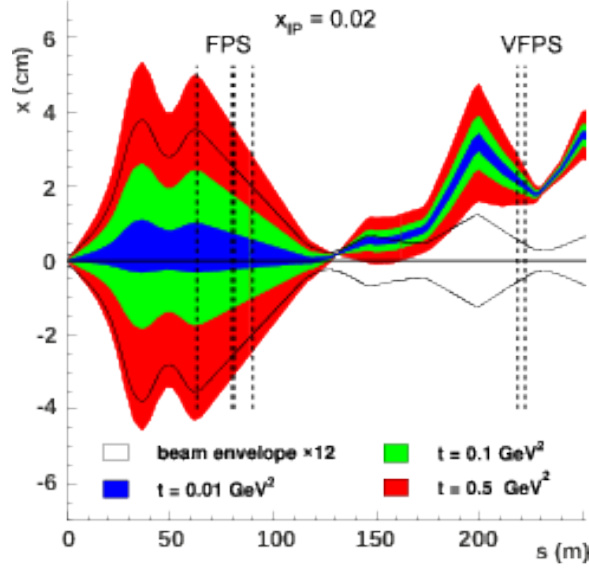


Figure 2.9: Beam envelope vs. distance to vertex in H1.

2.4.2 Wigner Distribution

One can use the Wigner distribution to tomographically image the internal structure of the nucleus [10]. The nucleus manifests different structures at varying momentum fractions; specifically, small momentum fractions exhibit gluon saturation [11]; see figure 2.10 for an illustration of how the nucleus appears at varying momentum fractions.

The quantum field theory lagrangian of the strong interaction is relatively simple, but because of confinement and asymptotic freedom the hadronic bound states are too complex for an analytic solution. Furthermore, collider experiment data requires a quantitative interpretation to be useful. The gap between QCD and heavy-ion data is bridged using the parton model, which considers hadrons as composed of quarks and gluons. Parton density functions (PDFs) model the longitudinal momentum distribution of the partons. PDFs are supplemented by transverse momentum distributions (TMDs) and generalized parton distributions (GPDs). In addition to transverse momentum, GPDs describe the transverse spatial distribution. TMDs and GPDs are derived from the final state particles of a collision. Markus Diehl maps the relationship between various distribution functions in figure 2.11 [12].

The Wigner distribution is a quantum phase space distribution that describes elliptic gluons

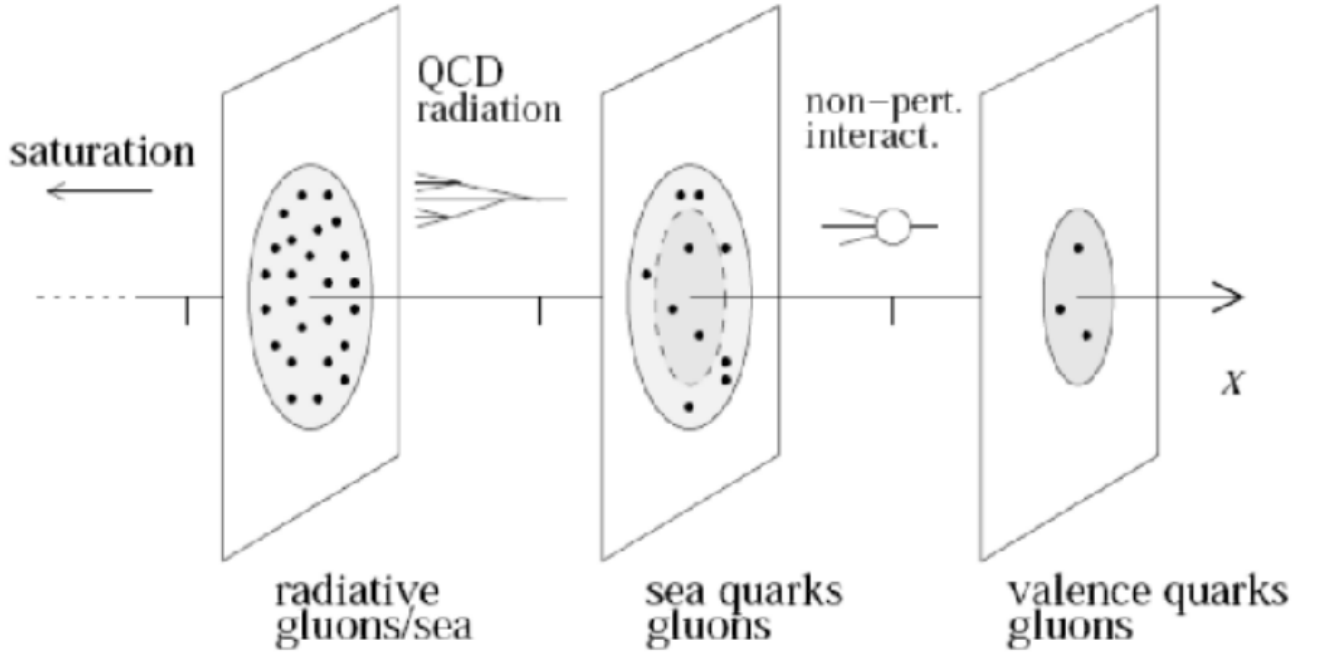


Figure 2.10: Subnuclear tomography

[13]. Specifically, by considering the color dipole scattering amplitude, the angular correlation of the nucleon recoil momentum and the dijet transverse momentum can provide a three-dimensional, tomographic image of the gluons within a high energy nucleus. This tomographic image takes the form of a Wigner distribution, which contains all the information of both TMDs and GPDs without violating the uncertainty principle. Specifically, the angular correlation directly measures the Fourier transform of the gluons. This is possible because the dipole amplitudes are functions of the impact parameter, and because collinear factorization holds.

TMDs and GPDs manifest non-perturbative QCD effects. The Wigner distribution, at this scale, reflects the relationship between the position and momentum of partons. Integrating the Wigner function over the transverse distance yields the TMD, while integrating over transverse momentum yields a GPD with spatial information.

Yoshitaka Hatta uses the dipole framework to show that the azimuthal angular correlations of coherent dijets are generated by the underlying gluon Wigner distribution. Furthermore, these correlations are consistent with predictions based on standard collinear factorization. Relevant

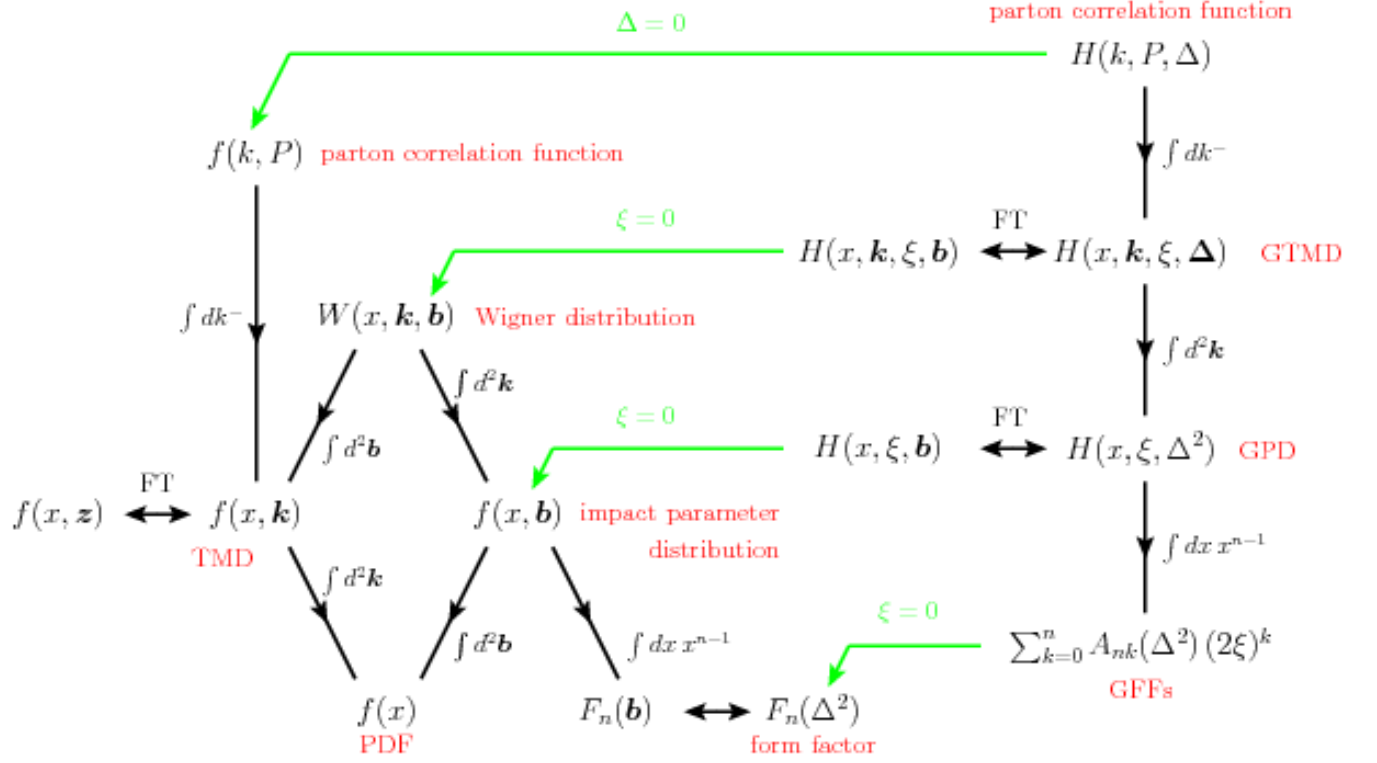


Figure 2.11: Interconnectedness of Parton Distributions.

kinematic variables are mapped in the figure 2.12.

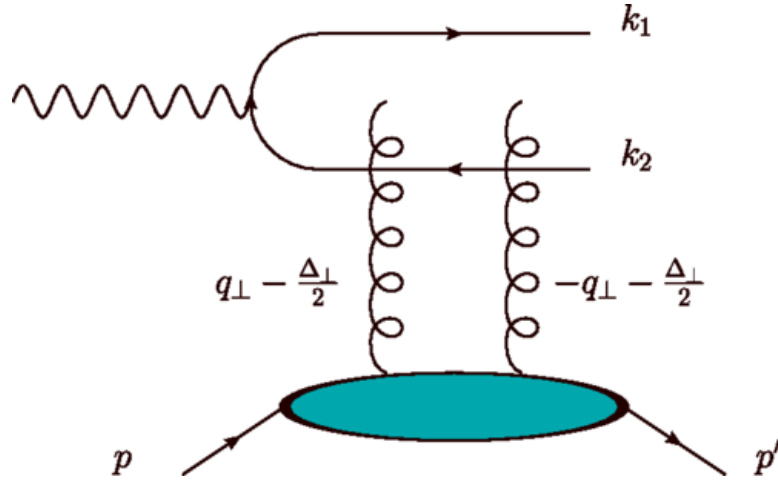


Figure 2.12: Feynman Diagram of Coherent Dijets in Dipole Framework.

It is expected that the dominant contribution to the angular correlation is the elliptic, corresponding to $n = 1$ in the Fourier transform.

Chapter 3

The Experiment

3.1 Large Hadron Collider

The Large Hadron Collider (LHC) has a radius of approximately 27 kilometers. As of this writing, it is the largest machine ever constructed. The initial purpose of the LHC was to discover the Higgs boson, but it is capable of investigating a variety of other physics phenomena, such as dark matter, extra-dimensions, and heavy-ion physics.

The beams are accelerated along a circular path using radio frequency cavities, gaining energy with each revolution. LHC is a hadron collider, meaning it is designed to collide particles made of quarks and gluons. The proton-proton, proton-Pb, and Pb-Pb collision energies are the largest ever probed experimentally. The LHC is a circular collider.

Heavy-ion collisions at LHC produce strongly interacting nuclear matter. The temperature and density of this matter is comparable to the state of the universe only a few milliseconds after the Big Bang.

3.1.1 ATLAS

"ATLAS" stands for "A Toroidal LHC ApparatuS". ATLAS was designed as a general purpose detector for LHC physics.

3.1.2 ALICE

"ALICE" stands for "A Large Ion Collider Experiment". ALICE was constructed for studying heavy-ion physics at the TeV scale.

3.1.3 LHCb

"LHCb" stands for "Large Hadron Collider beauty", reflecting the LHCb's purpose: b-quark ("beauty") studies. By examining CP violation in heavy-quark hadrons, LHCb hopes to elucidate the asymmetry of matter and antimatter.

3.1.4 TOTEM

"TOTEM" is a sub-experiment located at CMS. TOTEM uses Roman Pots, placed far forward of CMS, to measure the total proton+proton interaction cross-section. The differential cross-section, of proton-proton scattering, grows exponentially with the $|t|$ at low values of $|t|$. More precise measurements of this differential cross section can help distinguish between competing models of proton structure. Furthermore, the total interaction cross-section is an important benchmark for analyzing cosmic ray showers, and can be used to independently calibrate the beam luminosity measured at other LHC experiments. Diffractive studies at TOTEM complement those at CMS.

3.2 Compact Muon Solenoid

The Compact Muon Solenoid (CMS) is a general-purpose particle detector located at Point-5 of the LHC. CMS was designed to precisely measure the momentum of muons. The titular superconducting solenoid magnet was designed to generate a 4 Tesla field, but operates at 3.8 T to increase longevity. This field is homogeneous and parallel to the beam line close to the interaction point. The momentum of a muon is measured from how it deflects when moving through the magnetic field. Altogether, CMS weighs approximately 12,500 metric tons, with a diameter of 14.6 m and a length of 21.6 meters. Fig.3.1 displays the detector's various sub-systems.

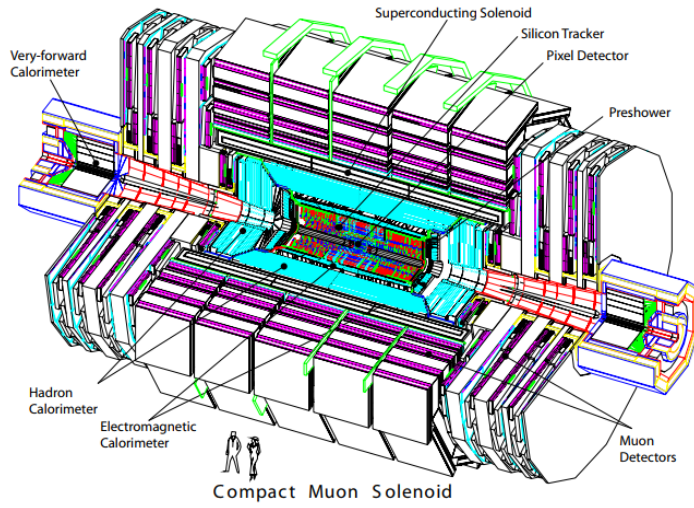


Figure 3.1: CMS Detector

Within the solenoid volume are a silicon pixel and strip tracker, a lead tungsten crystal electromagnetic calorimeter (ECAL), and a brass and scintillator hadron calorimeter (HCAL), each composed of a barrel and two endcap sections. Fig.3.2 radial layering of CMS component systems.

3.2.1 Tracker

The tracker measures the momentum of charged particles via their trajectory through a homogeneous magnetic field. The tracker consists of two units, the pixel tracker and the strip tracker, both of which are made of silicon. A charged particle causes an electrical signal when passing through a silicon pixel or silicon microstrip. CMS reconstructs these electrical signals, taken at specific points of position and time, into tracks. These tracks are accurate to 10 micrometers. The tracker is meant to have a particle pass all the way through it, with only minimal effect on particle's trajectory.

The tracker system is designed for high granularity and fast readout, such that each trajectory can be associated with its corresponding bunch crossing. The tracker is resilient enough to withstand the high flux of particles accompanying every bunch crossing; at design luminosity of $10^{34} \text{cm}^{-2} \text{s}^{-1}$, some 1000 particles will traverse the tracker every 25 ns. However, the mass of

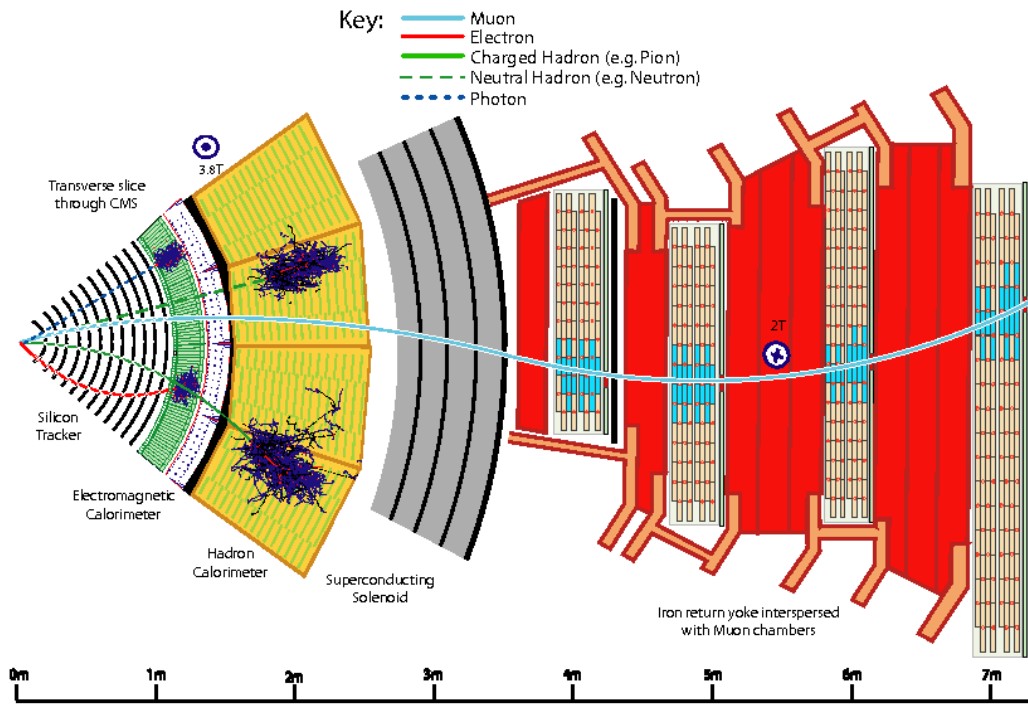


Figure 3.2: CMS radial cross-section

the tracker is minimal enough to suppress multiple scattering, off its material, that would distort particle trajectories. These design constraints – resistance and transparency – are satisfied silicon. The tracker has approximately $200m^2$ of silicon surface, making it the largest silicon detector ever constructed. The pseudorapidity coverage of the pixel and strip trackers is shown in fig.3.3.

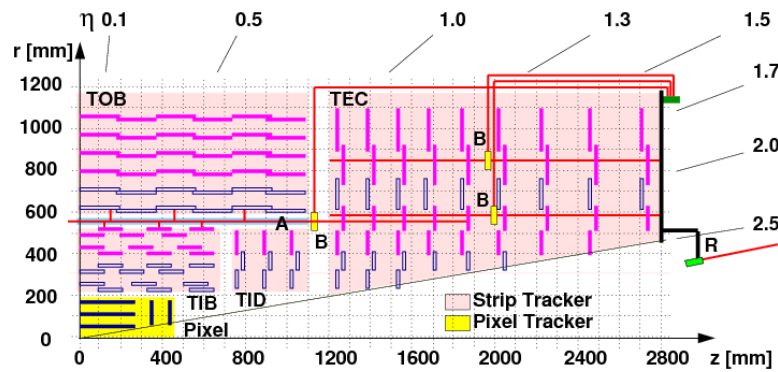


Figure 3.3: Pseudorapidity acceptance of tracker

3.2.1.1 Pixel Tracker

Every silicon-pixel has a corresponding readout chip. The readout chips are soldered through the bump-bonding method. The readout chip amplifies signals from the pixel. The pixel tracker is precise enough to distinguish the vertices of tracks originating from short-lived particles, such as bottomonia. The innermost elements of the pixel tracker come within 4.4 cms of the CMS interaction point. The pixel tracker covers a pseudorapidity range of $|\eta| < 2.5$ with some 66×10^6 separate pixels.

3.2.1.2 Strip Tracker

Outside the pixel tracker are the layers of the strip tracker. They function similar to the components of the pixel tracker, except the strip tracker consists of thin silicon plates. The strip tracker itself can be broken down into four components: the inner barrel layer, the inner endcaps, the outer barrel layer, and the outer endcaps. In total, these layers contain some 9.3×10^6 strips.

3.2.2 Electromagnetic Calorimeter

The Electromagnetic Calorimeter (ECAL) is the dedicated CMS calorimeter for detecting electrons and photons. The calorimeter is comprised of lead tungstate ($PbWO_4$) crystals arranged in cylinder about the beam, including two endcaps, as seen in fig3.4. The granularity of these crystals gives the ECAL excellent energy resolution, angular resolution, and spatial resolution; for example, the ECAL has the resolution suitable for the decay of the Higgs boson into two photons. The ECAL is both hermetic and homogenous.

The data readout is fast enough that CMS can trigger off signals in the ECAL. It takes about 25 ns for an ECAL hit to scintillate 80 percent of its lights, putting the calorimeter's rate on the same scale as the bunch crossing. Scintillation in the crystals activates photodetectors that transmit information to the L1 trigger. In the barrel these photodetectors are avalanche photodiodes (APDs). The endcaps use vacuum phototriodes (VPTs). ECAL's energy resolution, as a function of energy,

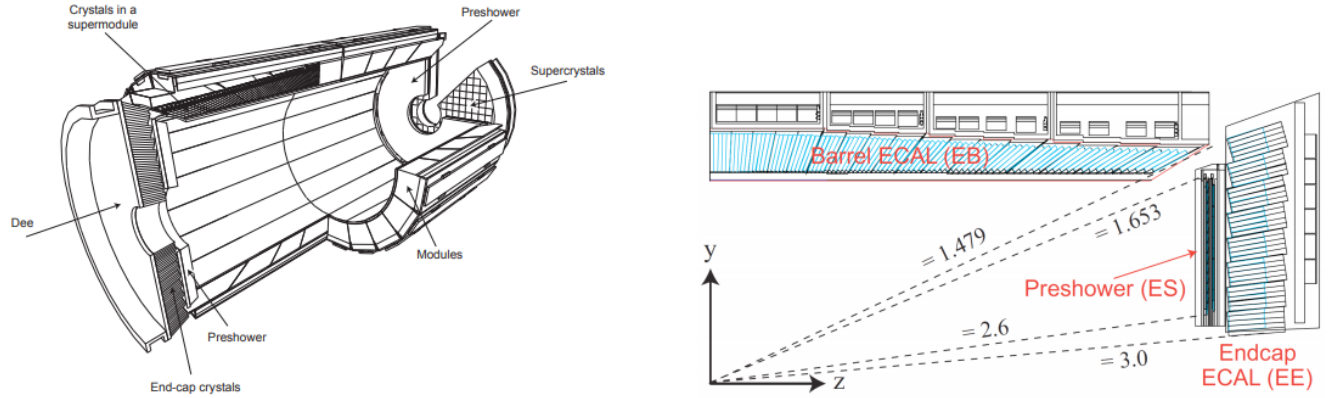


Figure 3.4: ECAL components

is given by fig.3.5. The resolution increases with energy because, at large energies, parton showers become more similar as their random fluctuations average-out.

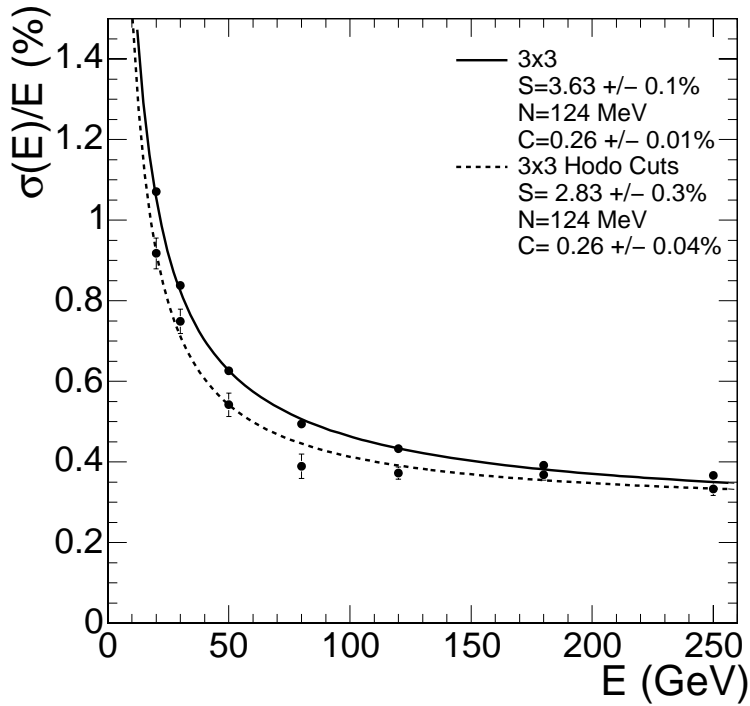


Figure 3.5: Ecal energy resolution

In CMS trigger development, "EG" triggers fire based on energy deposits in the ECAL; fig.3.6 gives the EG trigger energy resolution. This energy comes primarily from electrons and photons. When these particles strike a tungstate crystal, the particle shower size is approximately that of the crystal. Electrons are distinguished from photons by the correlation of track to ECAL energy. The

L1 trigger does not fire on tracks, which are reconstructed at the HLT level. Thus, L1 EG triggers do not distinguish between electrons and photons.

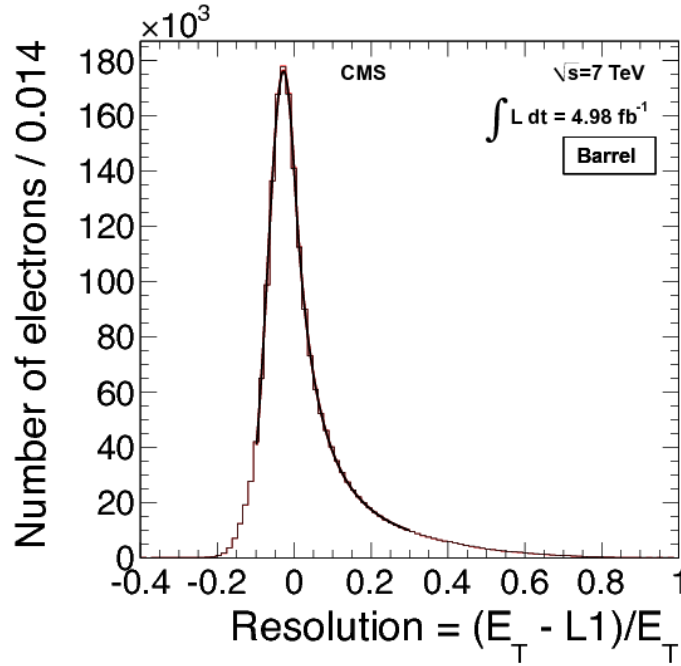


Figure 3.6: Ecal energy resolution

3.2.3 Hadronic Calorimeter

The Hadronic Calorimeter (HCAL) is the next layer outside the ECAL. The HCAL is a sampling calorimeter, meaning that it absorbs particles and measures their energy and momentum via scintillation. HCAL has such a large acceptance that it can indirectly observe non-interacting particles such as neutrinos. The HCAL is designed to be hermetic, so that imbalances of momentum and energy can be precisely measured. Fig.3.7 plots the HCAL's energy resolution; note that the reso-

lution changes with $|\eta|$.

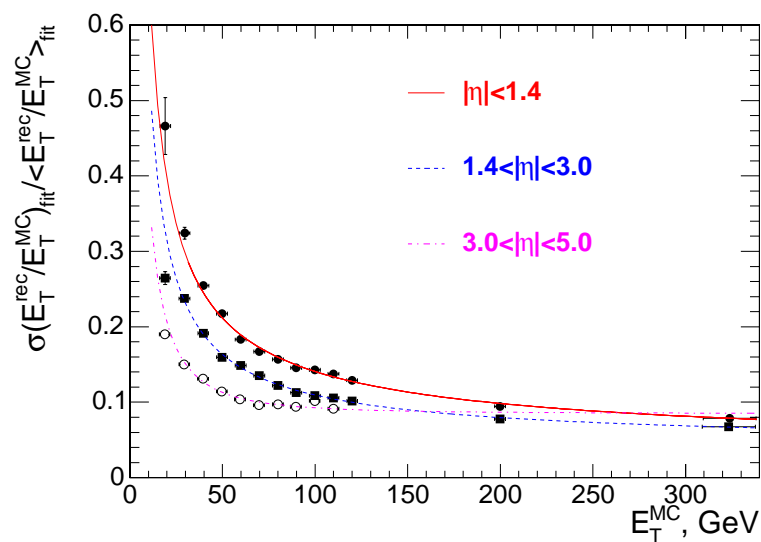


Figure 3.7: HCAL energy resolution

There are four sub-sections of the HCAL: the inner barrel (HB) and the outer barrel (HO), two endcaps (HE), and two forward calorimeters (HF). The HF are the most relevant to this analysis because of their use in triggering on non-hadronic events. Fig.3.8 shows the HCAL energy resolution.

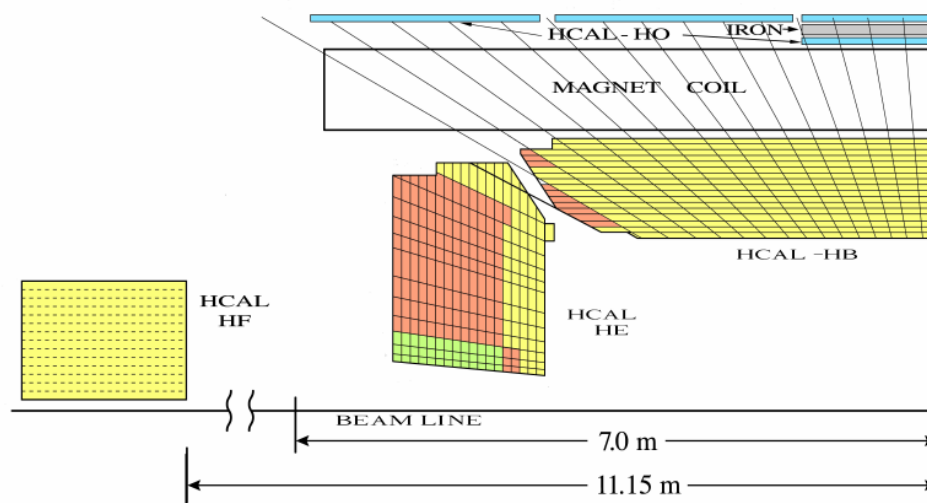


Figure 3.8: HCAL Components

3.2.3.1 Hadronic Forward Calorimeters

The Hadronic Forward Calorimeters (HF) absorbs the greatest portion of energy from collisions. As named, it is located in the forward region ($3.0 < |\eta| < 5.2$) of CMS and complements the coverage provided by the barrel and endcap detectors.

HCAL is made of quartz fibers and steel absorbers for maximum radiative resistance. When high energy particles pass through the quartz fibers, these particles are moving faster than the speed of light in the medium, depositing energy that causes particle showers. These showers give off light, in the form of Cherenkov radiation, that the fibers transmit to photomultiplier tubes (PMTs). The PMTs readout to the L1-trigger. Triggering on HF can also be done by vetoing on HF activity.

Hits in the HF are used to measure the instantaneous luminosity of CMS. As shown in fig.3.7, the HF have a finer E_T resolution than the other parts of the HCAL, making it suitable for high precision measurement of luminosity. Furthermore, because HF noise is comparatively small with respect to Minbias HF threshold, the veto of the HF threshold is a reliable measure of HF "emptiness".

3.2.4 Muon Detector

The outermost layer of CMS consists of the muon detectors, as seen in fig.3.9. Muons are particles nearly identical to electrons, except for their mass, which exceeds that of the electron by some two orders of magnitude. High mass particles, like the Higgs boson, often decay into a final state containing muons. The muon detector not only identifies muons, but also measures their momentum. The muon detector has readout fast enough for triggering on muons.

The muon detector consists of three types of component: muon drift tubes (DT), cathode strip chambers (CSC), and resistive plate chambers (RPC). The DTs are gas filled chambers that contain a stretched metal wire. When muons pass through the DT gas, electrons are excited. These electrons escape from the gas atoms and are attracted to the metal wire, which triggers a signal. The CSC, located in the endcaps, operate under similar principles, but contain perpendicular arrays of positively charged and negatively charged wires immersed in gas. The RPC do not use electrode

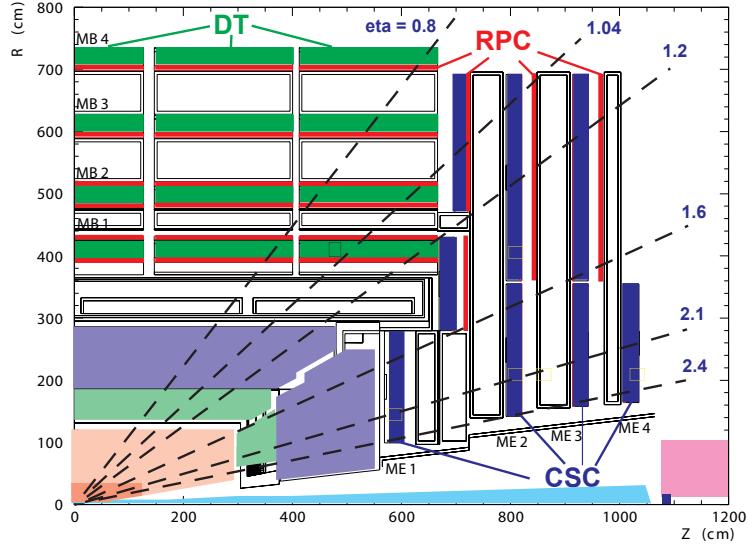


Figure 3.9: Pseudorapidity acceptance of muon detector

wires to detect excited electrons; instead, high-resistivity plates are used as alternating cathodes and anodes.

3.2.5 Zero Degree Calorimeter

The zero degree calorimeters are both sides of CMS, approximately 140 meters from the interaction point. Each ZDC consists of two independent systems: an electromagnetic calorimeter, for detecting very forward photons, and a hadronic calorimeter, for detecting neutrons. Because these neutrons result from the dissociation of nuclei, the ZDC can measure the centrality of heavy-ion collisions. Hadrons in the forward region have energy on the TeV scale, so the ZDC's hadronic calorimeter is made of thick tungsten plates. For a UPC process, the photon emitting nucleus is most likely to remain intact; therefore, ZDC data can the photon direction of a process, and by extension it's energy.

3.2.6 Particle Flow Algorithm

Raw data from the sub-detectors is combined, for data analysis, by the particle-flow (PF) algorithm. The PF takes the data about tracks in the tracker and energy deposits in the calorimeter,

and uses them to reconstruct physics-related data objects, like jets, and to identify specific particles, such as photons and muons. The PF also identifies missing energy and momentum for use in neutrino studies. These data objects are stored in a format similar to that of conventional MC event generators. CMS gains significant jet reconstruction efficiency via the PF. At low transverse momentum, PF reconstructs jets at nearly twice the resolution of HCAL and ECAL. This increase in efficiency comes from the PF integrating in track data with the calorimeter tower data. Fig.3.10 compares the performance of the PF algorithm to the calorimeter reconstruction.

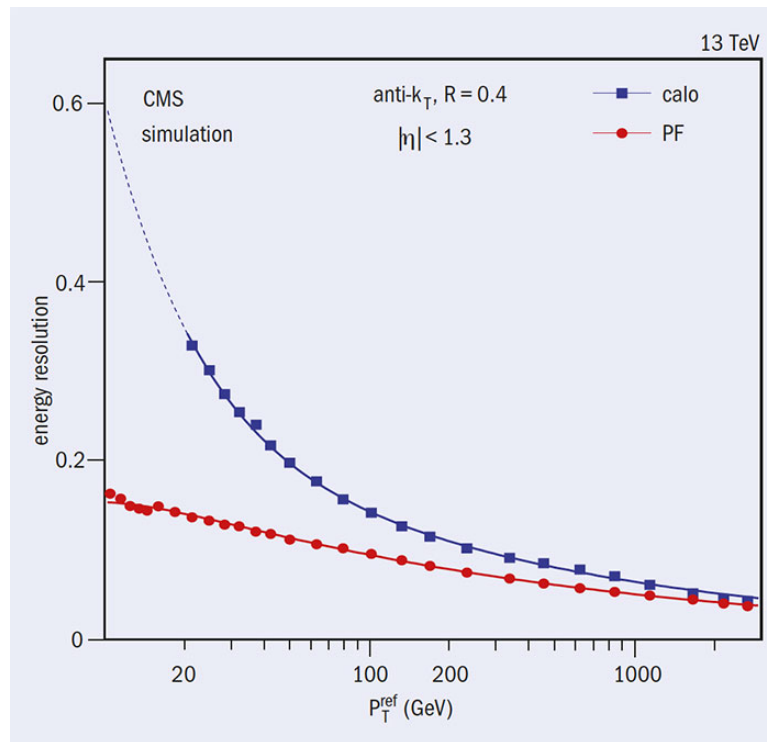


Figure 3.10: Performance of particle flow algorithm compared to calorimeter readout.

Chapter 4

Measuring Luminosity

4.1 Instantaneous Luminosity

One of the most important quantities measured by CMS is luminosity. Luminosity is necessary to convert the number of events detected, for a given channel, into a collision cross-section. Collision cross-sections are among the primary observables predicted by theoretical physics, specifically quantum field theory. For particle physics, the collision cross-section of a process is typically measured through the relation:

$$\sigma = \frac{R}{L}, \quad (4.1)$$

where σ is the cross-section, R is the rate at which the process occurs per collision, and L is the luminosity.

4.2 Luminometers

There are two kinds of CMS luminometer: online and offline. Online luminometers readout the luminosity per bunch in real time. As of 2015 there are three online luminometers: the pixel luminosity telescope (PLT), the HF, and the beam conditions monitor (BCM1f). There is a high-rate, independent data-acquisition system for each of the online luminometers. Offline luminometers measure the rate of reconstructed objects. The primary offline luminometer is the pixel tracker. In general, the offline luminometers have better stability over time. [14]

The online and offline luminometers complement each other for high precision data analysis. Specifically, the offline data can be used to calibrate out imperfections in the online data.

In addition to these hardware luminometers, CMS can use physics processes as luminosity benchmarks. For example, other experiments have measured the Z-boson cross-section to a high accuracy and high precision. Comparing this cross-section to the Z-boson mass-peak ,in CMS data, provides a cross-check to the delivered luminosity.

4.3 Van de Meer Scanning Calibration

The luminometers of CMS produce signals proportional to the instantaneous luminosity of the LHC beam. However, these signals need to be properly calibrated with respect to a known visible cross-section for each luminometer. This calibration is accomplished via Van de Meer scanning. The opposing beams of LHC are moved back and forth in the transverse plane. During the scan, the detector response is measured as a function of beam displacement. The beam widths are calculated from Gaussian fits to the detector response. The visible cross-section of the luminometer in question is then derived from the width of the beams, and acts as the calibration of the detector response.

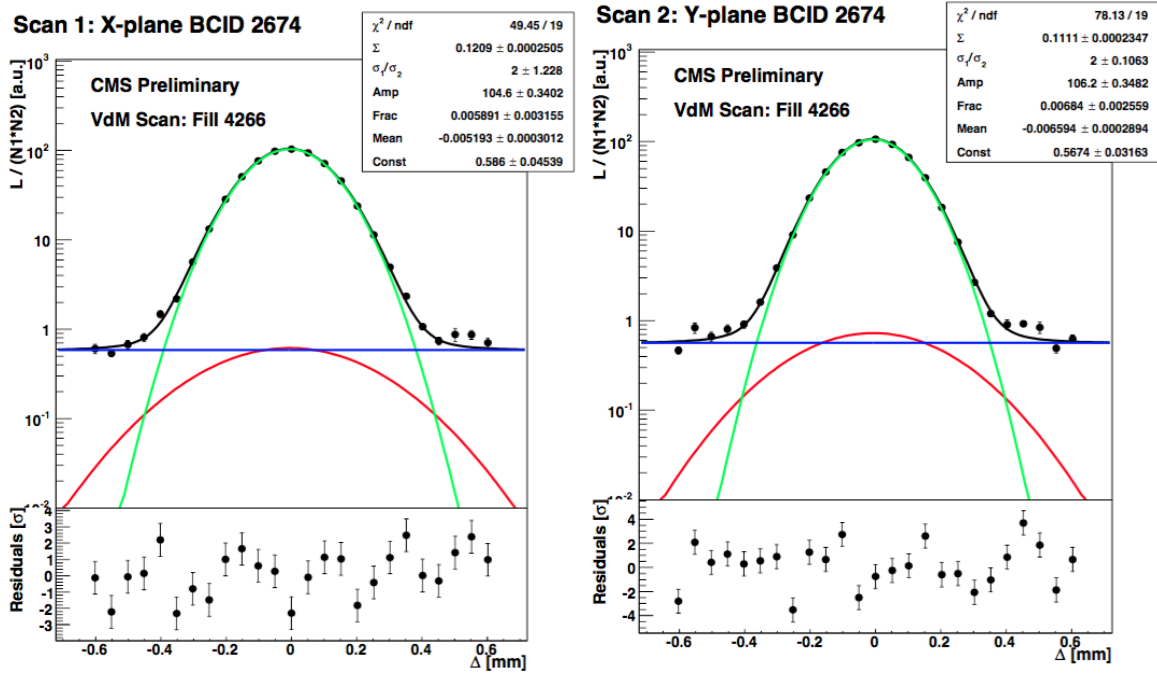


Figure 4.1: PCC VdM Scans.

4.4 Comparative Luminosity Performance of LHC Detectors

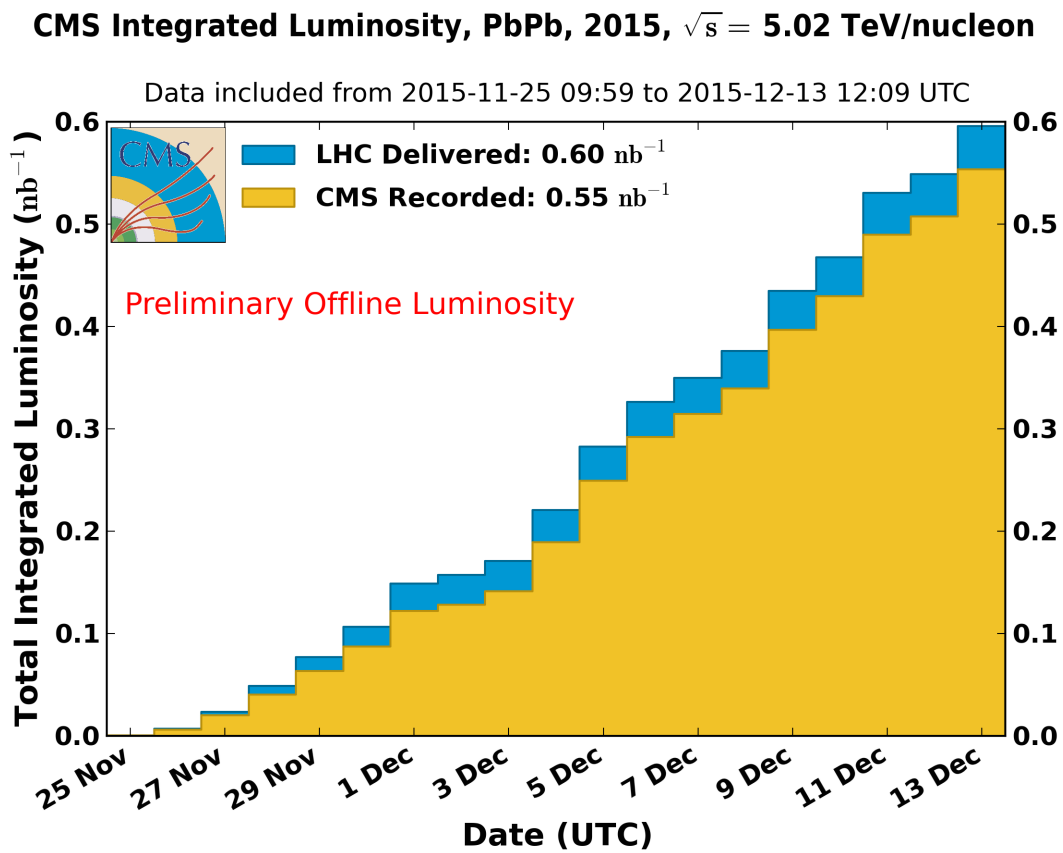


Figure 4.2: CMS lumi during HI-2015.

4.5 Systematic Uncertainty

4.6 My Contributions

I contributed to CMS luminosity validation, and performed studies on the long-term stability of the BRIL luminometers.

CMS Integrated Luminosity, pp

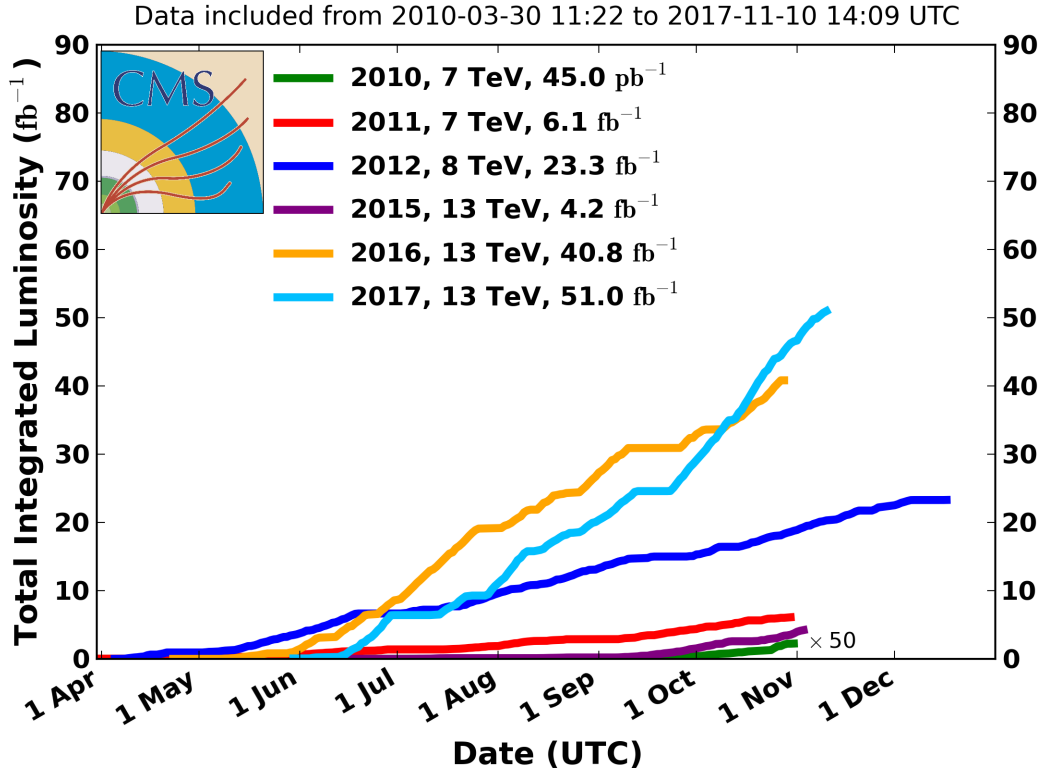


Figure 4.3: CMS Lumi by Era.

	Systematic	correction (%)	uncertainty (%)
Integration	Stability	-	1
	type 1	7 – 9	0.6
	type 2	0 – 4	0.7
	CMS deadtime	-	0.5
	Dynamic Inefficiency	-	0.4
Normalization	XY-Correlations	1.1	1.5
	Beam current calibration	-	0.3
	Ghosts and satellites	-	0.2
	Length scale	-3.2	1.5
	Orbit Drift	-	0.4
	Beam-beam deflection	1.8	0.4
	Dynamic- β	-	0.5
Total			2.7

Figure 4.4: Systematic Uncertainty During 2015 pp Run.

Fill	Begin Time YYYY.MM.DD HH:MM	Duration HH:MM	PeakInstLumi $\times 10^{30} \text{cm}^{-2} \text{s}^{-1} \text{pp}$ $\times 10^{24} \text{cm}^{-2} \text{s}^{-1} \text{Ions}$	DeliveredLumi $\text{pb}^{-1} \text{pp}$ $\mu\text{b}^{-1} \text{PbPb}$	RecordedLumi $\text{pb}^{-1} \text{pp}$ $\mu\text{b}^{-1} \text{PbPb}$	EffByLumi %
4658	2015.11.25 09:59	05:40	1	0.0	0.0	84.4
4659	2015.11.25 22:51	02:12	89	0.6	0.5	95.6
4661	2015.11.26 07:04	02:55	97	0.8	0.5	69.6
4664	2015.11.26 16:33	04:27	547	5.3	4.5	85.7
4666	2015.11.27 08:34	05:05	721	7.0	6.2	88.8
4669	2015.11.27 21:31	06:10	1327	16.1	12.8	79.2
4671	2015.11.28 11:13	09:03	1115	16.5	14.3	86.9
4672	2015.11.28 23:53	06:55	1085	14.0	11.9	84.6
4677	2015.11.29 17:42	06:54	1011	14.0	12.5	89.6
4679	2015.11.30 08:27	06:58	1092	14.5	12.9	88.8
4680	2015.11.30 21:17	05:13	1820	19.6	16.7	85.4
4681	2015.12.01 07:40	11:51	1856	28.4	25.1	88.2
4685	2015.12.02 05:39	03:28	1040	8.5	6.0	70.4
4688	2015.12.03 02:44	00:18	1887	1.9	1.0	51.1
4689	2015.12.03 09:03	09:04	1254	10.2	9.9	97.1
4690	2015.12.03 22:10	08:27	2030	22.0	21.7	98.5
4691	2015.12.04 12:51	07:31	2072	26.7	25.8	96.6
4692	2015.12.04 23:23	07:40	2334	30.3	29.7	98.1
4693	2015.12.05 10:22	00:60	2314	7.1	6.9	97.2
4695	2015.12.05 17:29	07:14	2216	27.8	26.2	94.3
4696	2015.12.06 07:03	05:29	1795	19.9	19.4	97.7
4697	2015.12.06 16:34	05:30	1879	20.5	20.1	98.2
4698	2015.12.07 01:41	00:09	2102	1.0	0.9	87.2
4699	2015.12.07 05:30	05:40	1885	21.5	20.4	94.8
4705	2015.12.08 05:37	02:24	183	1.1	1.1	97.8
4706	2015.12.08 11:08	04:32	2433	23.5	22.7	96.5
4709	2015.12.09 08:41	05:47	2161	23.3	22.8	97.8
4710	2015.12.09 17:42	05:52	2967	32.8	32.2	98.3
4711	2015.12.10 02:38	06:37	2886	31.6	31.1	98.4
4714	2015.12.11 01:20	06:39	2500	29.3	28.2	96.2
4715	2015.12.11 11:37	06:31	2559	30.6	29.3	95.7
4717	2015.12.11 23:00	10:21	0	0.0	0.0	0.0
4719	2015.12.12 17:26	04:36	2652	27.2	25.6	94.1
4720	2015.12.13 01:10	10:60	3036	44.9	44.2	98.5
Summary		199:09	3036	578.4	543.1	93.9

Figure 4.5: Luminosity by CMS fill.

Chapter 5

Trigger Development and Performance

5.1 Introduction to Triggering

Modern "triggering" methods began with Walther Bothe's development of the coincidence circuit. The coincidence circuit accepts two inputs. If these inputs are received within the same time window, approximating coincidence, the circuit passes an output. Bothe's originally used the coincidence circuit to take data for electron-photon production in Compton scattering.

5.2 Triggering at CMS

CMS uses a two-tiered triggering system. The first tier, the L1 trigger, is hardware based. The second tier, the high-level trigger (HLT), is software based. The L1 trigger receives raw data from the calorimeters and the muon detectors; this determines when the tracker will readout data. The raw data from the tracker, calorimeters, and muon detectors is then passed on to a computer farm running the HLT menu. The HLT then performs a simplistic reconstruction of the raw data into physics objects useful for analysis: jets, tracks, and identifiable particles. If an event passes the HLT, the raw data is permanently stored in preparation for a more complex reconstruction.

The 2015 UPC triggers were for low multiplicity events and low transverse momentum events. Typical heavy-ion collisions are high multiplicity events. Fig.5.1 is an event display of one of the first heavy-ion collisions at CMS in 2010.

Fig.5.3 is the event display of a UPC upsilon candidate.

For this analysis, the L1 trigger applies two selections. First, the L1 checks that at least one

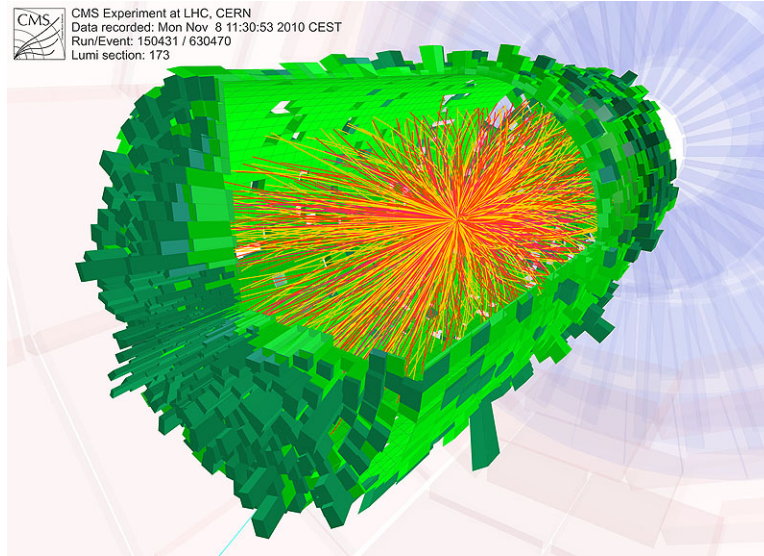


Figure 5.1: High multiplicity PbPb collision

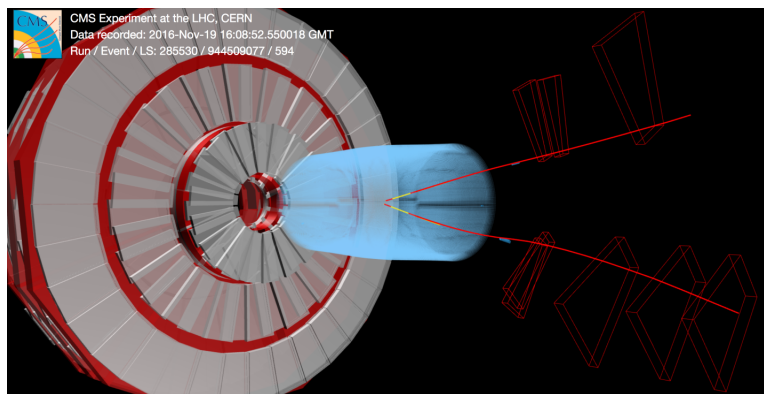


Figure 5.2: UPC Upsilon candidate

of the HF is empty. This is the most important part of the trigger in so far as it suppressed the hadronic contamination of the dataset. Then, if there is at least 5 GeV of energy deposited in the ECAL, the event passes to the HLT.

Low multiplicity events are difficult to distinguish from background. To compensate, the HLT in turn requires that there be at least once reconstructed track from the pixel tracker, to make sure that there are particles that will be reconstructed by the complete tracker. Only the pixel tracker is used for these HLTs to increase the speed of reconstruction while decreasing needed computer cycles.

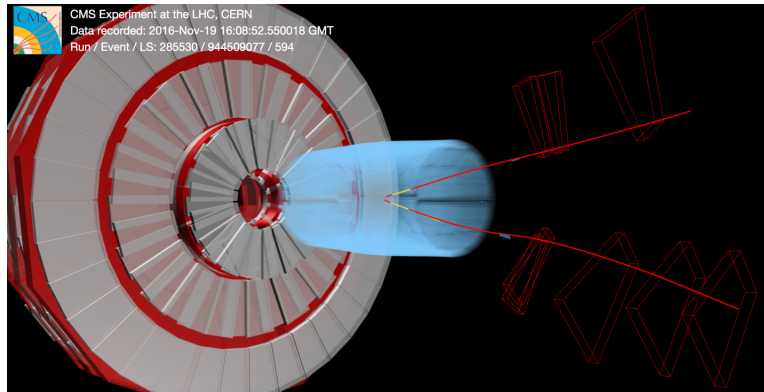


Figure 5.3: UPC Upsilon candidate

5.3 My Contributions

In preparation for the 2015 heavy-ion run, I prepared a high-level trigger menu. This trigger menu was optimized for firing on ultra-peripheral collisions. I tested the menu's performance on Monte Carlo generated by STARLIGHT and reconstructed through a GEANT4 simulation of CMS. During the experiment, I was present at CERN to monitor the trigger rates and deliver daily reports on their performance.

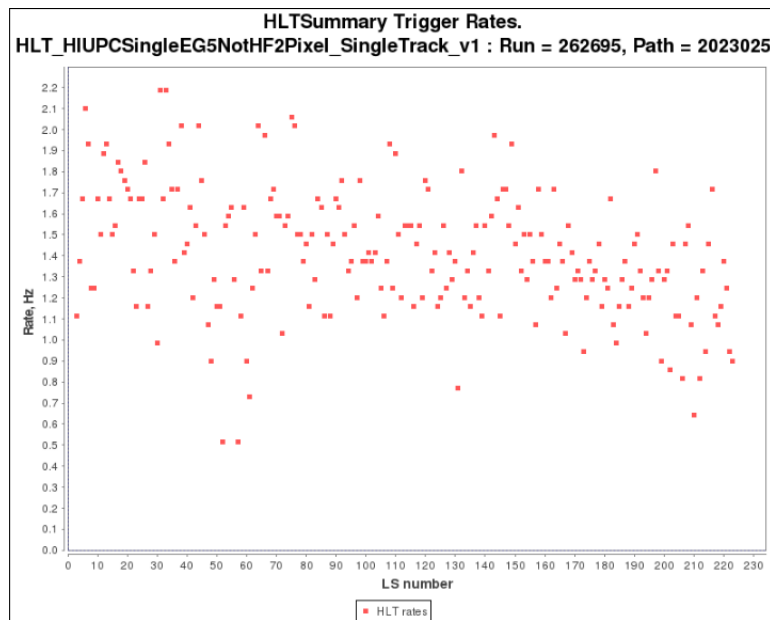


Figure 5.4: Example of trigger rate.

Chapter 6

Data Analysis

In this chapter our data sample will be analyzed according to the framework provided by Yoshikata Hatta. The angular correlation of jets is taken, and event mixing is used to factor out acceptance effects.

Chapter 7

Systematic Uncertainties

The primary sources of systematic uncertainty in this analysis are the measurements of track vertex, jet momentum, jet pseudorapidity, and HF energy.

Chapter 8

Results and Conclusions

In this chapter, the angular anisotropy of the elliptic gluons is compared to theoretical predictions from variations of NLO-QCD.

References

- [1] S. Bethke, “Experimental tests of asymptotic freedom,” *Prog. Part. Nucl. Phys.* **58** (2007) 351–386, [arXiv:hep-ex/0606035](#) [hep-ex].
- [2] J. D. Jackson, *Classical electrodynamics*. Wiley, New York, NY, 3rd ed. ed., 1999.
<http://cdsweb.cern.ch/record/490457>.
- [3] F. Halzen and A. D. Martin, *QUARKS AND LEPTONS: AN INTRODUCTORY COURSE IN MODERN PARTICLE PHYSICS*. 1984.
- [4] M. E. Peskin and D. V. Schroeder, *An Introduction to quantum field theory*. Addison-Wesley, Reading, USA, 1995.
<http://www.slac.stanford.edu/~mpeskin/QFT.html>.
- [5] D. Griffiths, *Introduction to elementary particles*. 2008.
- [6] CTEQ Collaboration, R. Brock *et al.*, “Handbook of perturbative QCD: Version 1.0,” *Rev. Mod. Phys.* **67** (1995) 157–248.
- [7] F. Wilczek, “QCD made simple,” *Phys. Today* **53N8** (2000) 22–28.
- [8] J. D. Bjorken, “Asymptotic Sum Rules at Infinite Momentum,” *Phys. Rev.* **179** (1969) 1547–1553.
- [9] H1 Collaboration, V. Andreev *et al.*, “Diffractive Dijet Production with a Leading Proton in ep Collisions at HERA,” *JHEP* **05** (2015) 056, [arXiv:1502.01683](#) [hep-ex].
- [10] Y. Hatta, B.-W. Xiao, and F. Yuan, “Probing the Small- x Gluon Tomography in Correlated Hard Diffractive Dijet Production in Deep Inelastic Scattering,” *Phys. Rev. Lett.* **116** no. 20, (2016) 202301, [arXiv:1601.01585](#) [hep-ph].

- [11] D. Boer *et al.*, “Gluons and the quark sea at high energies: Distributions, polarization, tomography,” arXiv:1108.1713 [nucl-th].
- [12] M. Diehl, “Generalized parton distributions,” *Phys. Rept.* **388** (2003) 41–277, arXiv:hep-ph/0307382 [hep-ph].
- [13] A. V. Belitsky, X.-d. Ji, and F. Yuan, “Quark imaging in the proton via quantum phase space distributions,” *Phys. Rev.* **D69** (2004) 074014, arXiv:hep-ph/0307383 [hep-ph].
- [14] CMS Collaboration, CMS, “Measurement of CMS Luminosity,”.
- [15] S. D. Ellis and D. E. Soper, “Successive combination jet algorithm for hadron collisions,” *Phys. Rev.* **D48** (1993) 3160–3166, arXiv:hep-ph/9305266 [hep-ph].
- [16] M. Thomson, *Modern particle physics*. Cambridge University Press, New York, 2013.
<http://www-spires.fnal.gov/spires/find/books/www?cl=QC793.2.T46::2013>.
- [17] H1 Collaboration, F. D. Aaron *et al.*, “Diffractive Dijet Photoproduction in ep Collisions at HERA,” *Eur. Phys. J.* **C70** (2010) 15–37, arXiv:1006.0946 [hep-ex].
- [18] F. D. Aaron *et al.*, “Measurement of the cross section for diffractive deep-inelastic scattering with a leading proton at HERA,” *Eur. Phys. J.* **C71** (2011) 1578, arXiv:1010.1476 [hep-ex].
- [19] ZEUS Collaboration, S. Chekanov *et al.*, “Deep inelastic scattering with leading protons or large rapidity gaps at HERA,” *Nucl. Phys.* **B816** (2009) 1–61, arXiv:0812.2003 [hep-ex].
- [20] J. A. Crittenden, “Exclusive production of neutral vector mesons at the electron - proton collider HERA,” arXiv:hep-ex/9704009 [hep-ex].
- [21] V. Guzey and M. Klasen, “A fresh look at factorization breaking in diffractive photoproduction of dijets at HERA at next-to-leading order QCD,” *Eur. Phys. J.* **C76** no. 8, (2016) 467, arXiv:1606.01350 [hep-ph].

- [22] V. Guzey and M. Klasen, “Diffractive dijet photoproduction in ultraperipheral collisions at the LHC in next-to-leading order QCD,” *JHEP* **04** (2016) 158, arXiv:1603.06055 [hep-ph].
- [23] **CMS Collaboration**, A. Benaglia, “The CMS ECAL performance with examples,” *JINST* **9** (2014) C02008.
- [24] J. Gaiser, “Charmonium Spectroscopy From Radiative Decays of the J/ψ and ψ' ,”.
- [25] S. van der Meer, “Calibration of the Effective Beam Height in the ISR,”.
- [26] T. Bauer, R. Spital, D. Yennie, and F. Pipkin, “The Hadronic Properties of the Photon in High-Energy Interactions,” *Rev.Mod.Phys.* **50** (1978) 261.
- [27] S. Donnachie, H. G. Dosch, O. Nachtmann, and P. Landshoff, “Pomeron physics and QCD,” *Camb.Monogr.Part.Phys.Nucl.Phys.Cosmol.* **19** (2002) 1–347.
- [28] **ALICE Collaboration** Collaboration, B. B. Abelev *et al.*, “Exclusive J/ψ photoproduction off protons in ultra-peripheral p-Pb collisions at $\sqrt{s_{NN}}=5.02$ TeV,” arXiv:1406.7819 [nucl-ex].
- [29] **ZEUS Collaboration** Collaboration, S. Chekanov *et al.*, “Exclusive photoproduction of J/ψ mesons at HERA,” *Eur.Phys.J.* **C24** (2002) 345–360, arXiv:hep-ex/0201043 [hep-ex].
- [30] **H1 Collaboration** Collaboration, A. Aktas *et al.*, “Elastic J/ψ production at HERA,” *Eur.Phys.J.* **C46** (2006) 585–603, arXiv:hep-ex/0510016 [hep-ex].
- [31] **H1 Collaboration** Collaboration, C. Alexa *et al.*, “Elastic and Proton-Dissociative Photoproduction of J/ψ Mesons at HERA,” *Eur.Phys.J.* **C73** (2013) 2466, arXiv:1304.5162 [hep-ex].

- [32] L. Frankfurt, M. Strikman, and M. Zhalov, “Elastic and large t rapidity gap vector meson production in ultraperipheral proton-ion collisions,” *Phys.Lett.* **B640** (2006) 162–169, arXiv:hep-ph/0605160 [hep-ph].
- [33] V. Guzey and M. Zhalov, “Rapidity and momentum transfer distributions of coherent J/ψ photoproduction in ultraperipheral pPb collisions at the LHC,” *JHEP* **1402** (2014) 046, arXiv:1307.6689 [hep-ph].
- [34] **ALICE Collaboration** Collaboration, B. Abelev *et al.*, “Coherent J/ψ photoproduction in ultra-peripheral Pb-Pb collisions at $\sqrt{s_{NN}} = 2.76$ TeV,” *Phys.Lett.* **B718** (2013) 1273–1283, arXiv:1209.3715 [nucl-ex].
- [35] K. Eskola, H. Paukkunen, and C. Salgado, “EPS09: A New Generation of NLO and LO Nuclear Parton Distribution Functions,” *JHEP* **0904** (2009) 065, arXiv:0902.4154 [hep-ph].
- [36] K. J. Eskola, H. Paukkunen, and C. A. Salgado, “An Improved global analysis of nuclear parton distribution functions including RHIC data,” *JHEP* **0807** (2008) 102, arXiv:0802.0139 [hep-ph].
- [37] J. Pumplin, D. Stump, J. Huston, H. Lai, P. M. Nadolsky, *et al.*, “New generation of parton distributions with uncertainties from global QCD analysis,” *JHEP* **0207** (2002) 012, arXiv:hep-ph/0201195 [hep-ph].
- [38] A. Martin, W. Stirling, R. Thorne, and G. Watt, “Parton distributions for the LHC,” *Eur.Phys.J.* **C63** (2009) 189–285, arXiv:0901.0002 [hep-ph].
- [39] M. Goldhaber and E. Teller, “On nuclear dipole vibrations,” *Phys.Rev.* **74** (1948) 1046–1049.
- [40] H. Steinwedel and J. H. D. Jensen, “,” *Zeits. f. Naturforsch* **5a** (1950) 343.

- [41] **ALICE Collaboration** Collaboration, E. Abbas *et al.*, “Charmonium and e^+e^- pair photoproduction at mid-rapidity in ultra-peripheral Pb-Pb collisions at $\sqrt{s_{NN}} = 2.76$ TeV,” *Eur.Phys.J.* **C73** (2013) 2617, arXiv:1305.1467 [nucl-ex].
- [42] H. Emling, “Electromagnetic excitation of the two phonon giant dipole resonance,” *Prog.Part.Nucl.Phys.* **33** (1994) 729–786.
- [43] E. de Passos, M. Hussein, L. Canto, and B. Carlson, “The Mean energy, strength and width of triple giant dipole resonances,” *Phys.Rev.* **C65** (2002) 034326, arXiv:nucl-th/0108002 [nucl-th].
- [44] M. Ryskin, “Diffractive J/ψ electroproduction in LLA QCD,” *Z.Phys.* **C57** (1993) 89–92.
- [45] V. Guzey, M. Strikman, and M. Zhalov, “Disentangling coherent and incoherent J/ψ photoproduction on nuclei by neutron tagging in ultraperipheral ion collisions at the LHC,” arXiv:1312.6486 [hep-ph].
- [46] L. Frankfurt, V. Guzey, and M. Strikman, “Leading Twist Nuclear Shadowing Phenomena in Hard Processes with Nuclei,” *Phys.Rept.* **512** (2012) 255–393, arXiv:1106.2091 [hep-ph].
- [47] V. Goncalves and M. Machado, “Vector Meson Production in Coherent Hadronic Interactions: An update on predictions for RHIC and LHC,” *Phys.Rev.* **C84** (2011) 011902, arXiv:1106.3036 [hep-ph].
- [48] A. Cisek, W. Schafer, and A. Szczurek, “Exclusive coherent production of heavy vector mesons in nucleus-nucleus collisions at LHC,” *Phys.Rev.* **C86** (2012) 014905, arXiv:1204.5381 [hep-ph].
- [49] T. Lappi and H. Mantysaari, “ J/ψ production in ultraperipheral Pb+Pb and p +Pb collisions at energies available at the CERN Large Hadron Collider,” *Phys.Rev.* **C87** no. 3, (2013) 032201, arXiv:1301.4095 [hep-ph].

- [50] J. Hufner, B. Kopeliovich, and A. B. Zamolodchikov, “Inelastic J / ψ photoproduction off nuclei: Gluon enhancement or double color exchange?,” *Z.Phys.* **A357** (1997) 113–120, [arXiv:nucl-th/9607033](#) [nucl-th].
- [51] S. J. Brodsky, L. Frankfurt, J. Gunion, A. H. Mueller, and M. Strikman, “Diffractive leptonproduction of vector mesons in QCD,” *Phys.Rev.* **D50** (1994) 3134–3144, [arXiv:hep-ph/9402283](#) [hep-ph].
- [52] M. Strikman, M. Tverskoy, and M. Zhalov, “Neutron tagging of quasielastic J/ ψ photoproduction off nucleus in ultraperipheral heavy ion collisions at RHIC energies,” *Phys.Lett.* **B626** (2005) 72–79, [arXiv:hep-ph/0505023](#) [hep-ph].
- [53] E. Witten, “Cosmic Separation of Phases,” *Phys.Rev.* **D30** (1984) 272–285.
- [54] R. Vogt, “Quark-Gluon Plasma Signatures,”.
- [55] C. von Weizsacker, “Radiation emitted in collisions of very fast electrons,” *Z.Phys.* **88** (1934) 612–625.
- [56] E. Williams, “Nature of the high-energy particles of penetrating radiation and status of ionization and radiation formulae,” *Phys.Rev.* **45** (1934) 729–730.
- [57] **CMS Collaboration** Collaboration, O. A. Grachov *et al.*, “Status of zero degree calorimeter for CMS experiment,” *AIP Conf.Proc.* **867** (2006) 258–265, [arXiv:nucl-ex/0608052](#) [nucl-ex].
- [58] **CMS HCAL Collaboration** Collaboration, G. Baatian *et al.*, “Design, Performance, and Calibration of CMS Hadron-Barrel Calorimeter Wedges,”.
- [59] C. Albajar, J. de Troconiz, J. Rohlf, and G. Wrochna, “Conceptual design of an improved CMS RPC muon trigger using the hadron outer scintillators,” *Nucl.Instrum.Meth.* **A545** (2005) 97–113.

- [60] **CMS Collaboration** Collaboration, S. Dasu *et al.*, “CMS. The TriDAS project. Technical design report, vol. 1: The trigger systems,”.
- [61] **CMS Collaboration** Collaboration, P. Sphicas, “CMS: The TriDAS project. Technical design report, Vol. 2: Data acquisition and high-level trigger,”.
- [62] S. Margetis, K. Safarik, and O. Villalobos Baillie, “Strangeness production in heavy-ion collisions,” *Ann.Rev.Nucl.Part.Sci.* **50** (2000) 299–342.
- [63] T. Matsui and H. Satz, “ J/ψ Suppression by Quark-Gluon Plasma Formation,” *Phys.Lett.* **B178** (1986) 416.
- [64] M. Gyulassy and M. Plumer, “Jet Quenching in Dense Matter,” *Phys.Lett.* **B243** (1990) 432–438.
- [65] A. Baltz, G. Baur, D. d’Enterria, L. Frankfurt, F. Gelis, *et al.*, “The Physics of Ultraperipheral Collisions at the LHC,” *Phys.Rept.* **458** (2008) 1–171, arXiv:0706.3356 [nucl-ex].
- [66] C. A. Bertulani, S. R. Klein, and J. Nystrand, “Physics of ultra-peripheral nuclear collisions,” *Ann.Rev.Nucl.Part.Sci.* **55** (2005) 271–310, arXiv:nucl-ex/0502005 [nucl-ex].
- [67] F. Karsch, E. Laermann, and A. Peikert, “Quark mass and flavor dependence of the QCD phase transition,” *Nucl.Phys.* **B605** (2001) 579–599, arXiv:hep-lat/0012023 [hep-lat].
- [68] S. Hands, “The Phase diagram of QCD,” *Contemp.Phys.* **42** (2001) 209–225, arXiv:physics/0105022 [physics.ed-ph].
- [69] L. Evans and P. Bryant, “LHC Machine,” *JINST* **3** (2008) S08001.

- [70] M. L. Miller, K. Reygers, S. J. Sanders, and P. Steinberg, “Glauber modeling in high energy nuclear collisions,” *Ann.Rev.Nucl.Part.Sci.* **57** (2007) 205–243, arXiv:nucl-ex/0701025 [nucl-ex].
- [71] G. Roland, K. Safarik, and P. Steinberg, “Heavy-ion collisions at the LHC,” *Prog.Part.Nucl.Phys.* **77** (2014) 70–127.
- [72] **CMS Collaboration** Collaboration, S. Chatrchyan *et al.*, “Multiplicity and transverse momentum dependence of two- and four-particle correlations in pPb and PbPb collisions,” *Phys.Lett.* **B724** (2013) 213–240, arXiv:1305.0609 [nucl-ex].
- [73] **ALICE Collaboration** Collaboration, B. Abelev *et al.*, “Long-range angular correlations on the near and away side in p -Pb collisions at $\sqrt{s_{NN}} = 5.02$ TeV,” *Phys.Lett.* **B719** (2013) 29–41, arXiv:1212.2001 [nucl-ex].
- [74] **ALICE Collaboration** Collaboration, K. Aamodt *et al.*, “The ALICE experiment at the CERN LHC,” *JINST* **3** (2008) S08002.
- [75] **ATLAS Collaboration** Collaboration, G. Aad *et al.*, “The ATLAS Experiment at the CERN Large Hadron Collider,” *JINST* **3** (2008) S08003.
- [76] **LHCb Collaboration** Collaboration, J. Alves, A. Augusto *et al.*, “The LHCb Detector at the LHC,” *JINST* **3** (2008) S08005.
- [77] J. Bjorken, “Highly Relativistic Nucleus-Nucleus Collisions: The Central Rapidity Region,” *Phys.Rev.* **D27** (1983) 140–151.
- [78] **STAR Collaboration** Collaboration, K. Ackermann *et al.*, “Elliptic flow in Au + Au collisions at $(S(NN))^{1/2} = 130$ GeV,” *Phys.Rev.Lett.* **86** (2001) 402–407, arXiv:nucl-ex/0009011 [nucl-ex].
- [79] J.-Y. Ollitrault, “Anisotropy as a signature of transverse collective flow,” *Phys.Rev.* **D46** (1992) 229–245.

- [80] P. Sorensen, “Elliptic Flow: A Study of Space-Momentum Correlations In Relativistic Nuclear Collisions,” arXiv:0905.0174 [nucl-ex].
- [81] N. Borghini, R. Bhalerao, and J. Ollitrault, “Anisotropic flow from Lee-Yang zeroes: A Practical guide,” *J.Phys.* **G30** (2004) S1213–S1216, arXiv:nucl-th/0402053 [nucl-th].
- [82] R. Bhalerao, N. Borghini, and J. Ollitrault, “Genuine collective flow from Lee-Yang zeroes,” *Phys.Lett.* **B580** (2004) 157–162, arXiv:nucl-th/0307018 [nucl-th].
- [83] N. Borghini, P. M. Dinh, and J.-Y. Ollitrault, “Flow analysis from cumulants: A Practical guide,” arXiv:nucl-ex/0110016 [nucl-ex].
- [84] V. Andreev, X. Aslanoglou, A. Azman, M. Bakirci, S. Basegmez, *et al.*, “Performance studies of a full-length prototype for the CASTOR forward calorimeter at the CMS experiment,” *Eur.Phys.J.* **C67** (2010) 601–615.
- [85] L. McLerran, “The Color Glass Condensate and Glasma,” arXiv:0804.1736 [hep-ph].
- [86] F. Gelis, “Color glass condensate and glasma,” *Nuclear Physics A* **854** no. 1, (2011) 10 – 17. <http://www.sciencedirect.com/science/article/pii/S0375947410006615>.
Saturation, the Color Glass Condensate and the Glasma: What Have We Learned from RHIC?
- [87] M. M. I. Bloch, E. J. A., E. D. Barge, C. Campagnari, P. Kalavase, V. Krutelyov, D. Kovalskyi, J. Ribnik, and N. Amapane, “Muon identification in cms,” *CMS Note* **2008/098** (2008) . <http://cdsweb.cern.ch/record/962045>.
- [88] L. Frankfurt, M. Strikman, and M. Zhalov, “Large t diffractive ρ -meson photoproduction with target dissociation in ultraperipheral p a and a a collisions at lhc,” hep-ph/0612072.
- [89] **H1** Collaboration, A. Aktas *et al.*, “Diffractive photoproduction of ρ mesons with large momentum transfer at hera,” *Phys. Lett.* **B638** (2006) 422–431, hep-ex/0603038.

- [90] **STAR** Collaboration, C. Adler *et al.*, “Coherent ρ^0 production in ultra-peripheral heavy ion collisions,” *Phys. Rev. Lett.* **89** (2002) 272302, nucl-ex/0206004.
- [91] T. Teubner, “Diffractive production of vector mesons and the gluon at small x ,” *AIP Conf. Proc.* **792** (2005) 416–419.
- [92] M. Klasen, “Hard photoproduction at hera,” hep-ph/0702052.
- [93] D. d’Enterria, “Hard spectra and qcd matter: Experimental review,” *J. Phys.* **G30** (2004) S767–S774, nucl-ex/0404018.
- [94] M. Strikman, R. Vogt, and S. White, “Probing small x parton densities in ultraperipheral a a and p a collisions at the lhc,” *Phys. Rev. Lett.* **96** (2006) 082001, hep-ph/0508296.
- [95] J. Nystrand, “Electromagnetic interactions in nucleus nucleus and proton proton collisions,” *Nucl. Phys.* **A752** (2005) 470–479, hep-ph/0412096.
- [96] S. R. Klein and J. Nystrand, “Photoproduction of quarkonium in proton proton and nucleus nucleus collisions,” *Phys. Rev. Lett.* **92** (2004) 142003, hep-ph/0311164.
- [97] A. J. Baltz, S. R. Klein, and J. Nystrand, “Coherent vector meson photoproduction with nuclear breakup in relativistic heavy ion collisions,” *Phys. Rev. Lett.* **89** (2002) 012301, nucl-th/0205031.
- [98] S. Klein and J. Nystrand, “Exclusive vector meson production in relativistic heavy ion collisions,” *Phys. Rev.* **C60** (1999) 014903, hep-ph/9902259.
- [99] L. Frankfurt, M. Strikman, and C. Weiss, “Small- x physics: From hera to lhc and beyond,” *Ann. Rev. Nucl. Part. Sci.* **55** (2005) 403–465, hep-ph/0507286.
- [100] V. P. Goncalves and M. V. T. Machado, “Heavy quarks and meson production in ultraperipheral heavy ion collisions,” hep-ph/0601131.
- [101] B. L. Berman and S. C. Fultz *Rev. Mod. Phys.* **47** (1975) 713.

- [102] R. Vogt, “Heavy quark production in heavy ion colliders,” *Heavy Ion Phys.* **18** (2003) 11–20, hep-ph/0205330.
- [103] K. Piotrkowski, “Tagging two-photon production at the lhc,” *Phys. Rev.* **D63** (2001) 071502, hep-ex/0009065.
- [104] M. W. Krasny, J. Chwastowski, and K. Slowikowski, “Luminosity measurement method for lhc: The theoretical precision and the experimental challenges,” hep-ex/0610052.
- [105] **Particle Data Group** Collaboration, W.-M. Yao *et al.*, “Review of particle physics,” *J. Phys.* **G33** (2006) 1–1232.
- [106] V. A. Khoze, A. D. Martin, and M. G. Ryskin, “Double-diffractive processes in high-resolution missing- mass experiments at the tevatron,” *Eur. Phys. J.* **C19** (2001) 477–483, hep-ph/0011393.
- [107] M. Albrow, 2001. private communication.
- [108] I. A. Pshenichnov, J. P. Bondorf, I. N. Mishustin, A. Ventura, and S. Masetti, “Mutual heavy ion dissociation in peripheral collisions at ultrarelativistic energies,” *Phys. Rev.* **C64** (2001) 024903, nucl-th/0101035.
- [109] M. Boonekamp *et al.* Atl-gen-2004-001, March, 2004.
- [110] S. Baffioni, C. Charlot, *et al.*, “Electron reconstruction in cms,” *CMS NOTE* 2006/40 (2006) .
- [111] P. Yepes, “Studying light objects in ultra-peripheral heavy ion collisions,” *CMS NOTE* 2003/022 (2003) .
- [112] A. Lardeux, “ J/ψ production in Pb-Pb collisions at $\sqrt{s_{NN}}=2.76$ TeV in the ALICE experiment,” *J.Phys.Conf.Ser.* **446** (2013) 012042.

- [113] S. Chatrchyan *et al.*, “The cms experiment at the cern lh,” *Journal of Instrumentation* **3** no. 08, (2008) S08004. <http://stacks.iop.org/1748-0221/3/i=08/a=S08004>.
- [114] M. B. G. Ducati, M. T. Griep, and M. V. T. Machado, “Exclusive photoproduction of j/ψ and $\psi(2s)$ states in proton-proton collisions at the cern lh,” Tech. Rep. arXiv:1305.4611, May, 2013. Comments: 04 pages, 2 figures. arXiv admin note: text overlap with arXiv:1305.2407.
- [115] E. Fermi, “On the Theory of Collisions between Atoms and Electrically Charged Particles,” in *Electromagnetic Probes of Fundamental Physics*, W. Marciano and S. White, eds., pp. 243–252. Sept., 2003. hep-th/0205086.
- [116] **PHENIX Collaboration** Collaboration, A. Adare *et al.*, “Cold Nuclear Matter Effects on J/ψ Yields as a Function of Rapidity and Nuclear Geometry in Deuteron-Gold Collisions at $\sqrt{s_{NN}} = 200$ GeV,” *Phys.Rev.Lett.* **107** (2011) 142301, arXiv:1010.1246 [nucl-ex].
- [117] C. A. Brau, *Modern Problems in Classical Electrodynamics*. Oxford, New York, NY, 1st ed. ed., 2004.
- [118] S. R. Klein and J. Nystrand, “Exclusive vector meson production in relativistic heavy ion collisions,” *Phys. Rev. C* **60** (Jun, 1999) 014903.
<http://link.aps.org/doi/10.1103/PhysRevC.60.014903>.
- [119] S. R. Klein and J. Nystrand, “Interference in exclusive vector meson production in heavy-ion collisions,” *Phys. Rev. Lett.* **84** (Mar, 2000) 2330–2333.
<http://link.aps.org/doi/10.1103/PhysRevLett.84.2330>.
- [120] V. Rebyakova, M. Strikman, and M. Zhalov, “Coherent rho and J/ψ photoproduction in ultraperipheral processes with electromagnetic dissociation of heavy ions at RHIC and LHC,” *Phys.Lett.* **B710** (2012) 647–653, arXiv:1109.0737 [hep-ph].

- [121] V. Rebyakova, M. Strikman, and M. Zhalov, “Coherent ρ and J/Ψ photoproduction in ultraperipheral processes with electromagnetic dissociation of heavy ions at RHIC and LHC,” *Physics Letters B* **710** no. 4–5, (2012) 647 – 653.
<http://www.sciencedirect.com/science/article/pii/S0370269312003152>.
- [122] V. Guzey, E. Kryshen, M. Strikman, and M. Zhalov, “Evidence for nuclear gluon shadowing from the ALICE measurements of pbbp ultraperipheral exclusive production,” *Physics Letters B* **726** no. 1–3, (2013) 290 – 295.
<http://www.sciencedirect.com/science/article/pii/S0370269313006825>.
- [123] A. Adeluyi and C. A. Bertulani, “Gluon distributions in nuclei probed at energies available at the CERN large hadron collider,” *Phys. Rev. C* **84** (Aug, 2011) 024916.
<http://link.aps.org/doi/10.1103/PhysRevC.84.024916>.
- [124] A. Adeluyi and T. Nguyen, “Coherent photoproduction of ψ and Υ mesons in ultraperipheral pPb and PbPb collisions at the CERN Large Hadron Collider at $\sqrt{s_{NN}} = 5$ TeV and $\sqrt{s_{NN}} = 2.76$ TeV,” *Phys. Rev. C* **87** (Feb, 2013) 027901, arXiv:1302.4288 [nucl-th]. <http://link.aps.org/doi/10.1103/PhysRevC.87.027901>.
- [125] T. C. collaboration, “Performance of cms muon reconstruction in pp collision events at $\sqrt{s} = 7$ tev,” *Journal of Instrumentation* **7** no. 10, (2012) P10002.
<http://stacks.iop.org/1748-0221/7/i=10/a=P10002>.
- [126] **CMS Collaboration** Collaboration, S. Chatrchyan *et al.*, “Measurement of CMS Luminosity,”.
- [127] **CMS Collaboration** Collaboration, G. Bayatian *et al.*, “CMS technical design report, volume II: Physics performance,” *J.Phys.* **G34** (2007) 995–1579.
- [128] **CMS Collaboration** Collaboration, *The CMS tracker: addendum to the Technical Design Report*. Technical Design Report CMS. CERN, Geneva, 2000.

- [129] P. Faccioli, C. Lourenco, J. Seixas, and H. K. Wohri, “Towards the experimental clarification of quarkonium polarization,” *Eur.Phys.J.* **C69** (2010) 657–673, [arXiv:1006.2738 \[hep-ph\]](#).
- [130] J. Alwall, A. Ballestrero, P. Bartalini, S. Belov, E. Boos, *et al.*, “A Standard format for Les Houches event files,” *Comput.Phys.Comm.* **176** (2007) 300–304, [arXiv:hep-ph/0609017 \[hep-ph\]](#).
- [131] T. Sjöstrand, S. Mrenna, and P. Skands, “Pythia 6.4 physics and manual,” *Journal of High Energy Physics* **2006** no. 05, (2006) 026.
<http://stacks.iop.org/1126-6708/2006/i=05/a=026>.
- [132] P. Steinberg, “Relativistic heavy ion physics: Results from AGS to RHIC,” *eConf* **C020620** (2002) FRBT03, [arXiv:nucl-ex/0210009 \[nucl-ex\]](#).
- [133] H. Satz, “The SPS heavy ion programme,” *Phys.Rept.* **403-404** (2004) 33–50, [arXiv:hep-ph/0405051 \[hep-ph\]](#).
- [134] M. Chiu, A. Denisov, E. Garcia, J. Katzy, A. Makeev, M. Murray, and S. White, “Measurement of mutual coulomb dissociation in $\sqrt{s_{\text{NN}}} = 130\text{GeV}$ $au + au$ collisions,” *Phys. Rev. Lett.* **89** (Jun, 2002) 012302.
<http://link.aps.org/doi/10.1103/PhysRevLett.89.012302>.
- [135] M. Wilde, “Measurement of direct photons in pp and pb–pb collisions with {ALICE},” *Nuclear Physics A* **904–905** no. 0, (2013) 573c – 576c.
<http://www.sciencedirect.com/science/article/pii/S0375947413001954>. The Quark Matter 2012 Proceedings of the {XXIII} International Conference on Ultrarelativistic Nucleus-Nucleus Collisions.
- [136] J. D. Bjorken, “Highly relativistic nucleus-nucleus collisions: The central rapidity region,” *Phys. Rev. D* **27** (Jan, 1983) 140–151.
<http://link.aps.org/doi/10.1103/PhysRevD.27.140>.

- [137] P. Stankus, “Direct photon production in relativistic heavy-ion collisions,” *Annual Review of Nuclear and Particle Science* **55** no. 1, (2005) 517–554,
<http://dx.doi.org/10.1146/annurev.nucl.53.041002.110533>.
<http://dx.doi.org/10.1146/annurev.nucl.53.041002.110533>.
- [138] H. Song, S. A. Bass, U. Heinz, T. Hirano, and C. Shen, “200 *a* gev Au + Au collisions serve a nearly perfect quark-gluon liquid,” *Phys. Rev. Lett.* **106** (May, 2011) 192301.
<http://link.aps.org/doi/10.1103/PhysRevLett.106.192301>.
- [139] B. Alver *et al.*, “Importance of correlations and fluctuations on the initial source eccentricity in high-energy nucleus-nucleus collisions,” *Phys. Rev. C* **77** (Jan, 2008) 014906. <http://link.aps.org/doi/10.1103/PhysRevC.77.014906>.
- [140] A. J. Baltz, C. Chasman, and S. N. White, “Correlated forward–backward dissociation and neutron spectra as a luminosity monitor in heavy-ion colliders,” *Nuclear Instruments and Methods in Physics Research Section A: Accelerators, Spectrometers, Detectors and Associated Equipment* **417** no. 1, (1998) 1 – 8.
<http://www.sciencedirect.com/science/article/pii/S0168900298005750>.
- [141] I. A. Pshenichnov, J. P. Bondorf, I. N. Mishustin, A. Ventura, and S. Masetti, “Mutual heavy ion dissociation in peripheral collisions at ultrarelativistic energies,” *Phys. Rev. C* **64** (Jul, 2001) 024903. <http://link.aps.org/doi/10.1103/PhysRevC.64.024903>.
- [142] I. A. Pshenichnov, I. N. Mishustin, J. P. Bondorf, A. S. Botvina, and A. S. Iljinov, “Particle emission following coulomb excitation in ultrarelativistic heavy-ion collisions,” *Phys. Rev. C* **60** (Sep, 1999) 044901. <http://link.aps.org/doi/10.1103/PhysRevC.60.044901>.
- [143] P. Chomaz, “Collective excitations in nuclei.”
- [144] <http://starlight.hepforge.org>.

[145] S. Chatrchyan *et al.*, “ J/ψ and $\psi(2s)$ production in pp collisions at $\sqrt{s} = 7$ tev,” *Journal of High Energy Physics* **2012** no. 2, (2012) .

<http://dx.doi.org/10.1007/JHEP02%282012%29011>.

Appendix A

My Appendix, Next to my Spleen

There could be lots of stuff here